Department of Precision and Microsystems Engineering

Simulating an Acoustic Cavity for Single Pixel Photoacoustic Imaging

Chris Bootsma

Report no : 2024.045
Coach : Dr.ir. S. Iskander-Rizk
Professor : Dr.ir. S. Iskander-Rizk
Specialisation : OPT
Type of report : Master Thesis
Date : 01-07-2024

Master thesis

Simulating an Acoustic Cavity for Single Pixel Photoacoustic Imaging

Chris Bootsma

Delft University of Technology

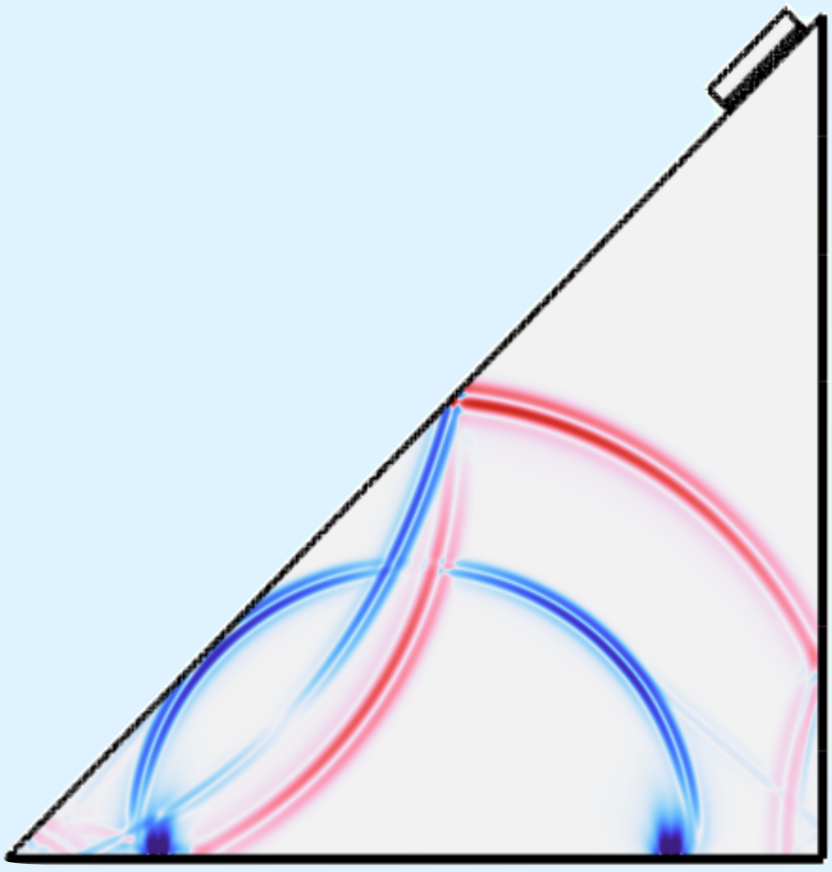

TU Delft

Master thesis

Simulating an Acoustic Cavity for Single Pixel Photoacoustic Imaging

by

Chris Bootsma

Student Name	Student Number
Chris Bootsma	5188032

Supervisor: Dr.ir. S. Iskander-Rizk
Faculty: Mechanical, Maritime and Materials Engineering, Delft
Department: Precision and Microsystems Engineering (PME)

Style: TU Delft Report Style, with modifications by Daan Zwaneveld

TU Delft

Preface

This Master's thesis was written as part of the Master's in Mechanical Engineering at the faculty of ME of the Technical University of Delft. For the past months, I have been working on a COMSOL model that can simulate a novel photoacoustic imaging technique. The result can be found in this report. Since I have enjoyed working on this project, I hope you will enjoy reading it.

Chris Bootsma
Delft, July 2024

Summary

The objective of this master's thesis is to develop a numerical model that simulates the measurement of elastic waves within a solid domain generated by the photoacoustic (PA) effect. The model may facilitate the development of a novel, forward-looking PA endoscope that integrates a relatively new PA imaging method for the first time. PA endoscopy is used for imaging the tissue layers up to several millimeters deep, with applications including intravascular imaging and imaging of the gastrointestinal tract. The most challenging requirement is achieving a frame rate exceeding 20 Hz while maintaining a reasonable resolution. Recently, novel imaging techniques, such as photoacoustic topography through an ergodic relay (PATER) [29], have been explored based on a single sensor, which reduces complexity and speeds up frame rates. To facilitate the design of this novel PA endoscope a numerical model could be beneficial. However, the modelling of this process is not straightforward due to the time dependency and high frequencies involved.

A model has been built in COMSOL; an important aspect of this model is a highly tunable but representative load distribution. The ability to change the input signal length such that the frequency content is not more than what could be measured allows for using a mesh size that is not smaller than necessary. The interface used in COMSOL can simulate elastic waves and can be coupled to other interfaces such as pressure waves, electrostatics, and heat transfer. The load distribution can be modified such that a single PA source is simulated or multiple sources are simulated simultaneously. Both the calibration and imaging modes can thus be tested.

The mesh size of the model was tuned using a mesh convergence study. Pearson's product-moment correlation coefficient r and the root mean square (rms) were used to measure convergence. The model was validated using an experimental dataset from PATER. Validation was done through a visualisation of the elastic waves, a visual comparison of the measurement results, a comparison of frequency spectra and a comparison of the cross-correlation map. Since computational costs are very important for the useability of the model, an overview is made of the performance of all simulations. In addition, a study was conducted to find the scaling of the computation time when more cores are used on a cluster.

The 2D model can be used to quantify performance parameters of the new design. The options within COMSOL allow for extending the model to investigate different aspects. Since the dimensions of the new endoscope are small, 3D models can also be used if the computational resources are sufficient. Fortunately, an old workstation might already be sufficient.

Contents

Nomenclature

Abbreviations

Abbreviation	Definition
DOV	depth of view
FOV	field of view
SMF	single mode fiber
MMF	multimode fiber
PRR	Pulse repetition rate
PA	photoacoustic
PATER	photoacoustic topography through an ergodic relay
PAI	photoacoustic imaging
PACTER	photoacoustic computed tomography through an ergodic relay
PACT	photoacoustic computed tomography
PAM	photoacoustic microscopy
US	ultrsound
TWIST	two-step iterative shrinkage thresholding
ER	ergodic relay
FISTA	fast iterative shrinkage thresholding algorithm
SPL	sound pressure level
epw	elements per wavelength
FWHM	full width at half maximum
DG-FEM	discontinuous Galerkin finite element method
RR	ratio of root mean square
rms	root mean square

Symbols

Symbol	Definition	Unit
$N_{samples}$	number of measurement points	
f_{Cmax}	maximum C-scan rate	[Hz]
f_{Cfast}	C-scan rate closest to real time imaging or 20[Hz]	
PRR_{Cfast}	PRR_{crit} or PRR needed for 20[Hz]	
pa	pulse averaging number	[-]
c	speed of sound	$[\mathrm{m\,s^{-1}}]$
d	target imaging depth	[m]
β	thermal coefficient of volume expansion	
p	pressure	$[\mathrm{N\,m^{-1}\,m^{2}}]$
C_p	specific heat capacity at constant pressure	
H	heating function	
Φ	optical fluence rate	
η	percentage of optical energy converted into heat	[-]
μ_a	optical absorption coefficient	
c_p	longitudinal fluid wave speed	$[\mathrm{m\,s^{-1}}]$
c_1	longitudinal wave speed	$[\mathrm{m\,s^{-1}}]$
c_2	transverse wave speed	$[\mathrm{m\,s^{-1}}]$

Symbol	Definition	Unit
c_R	rayleigh wave speed	[m s^{-1}]
E	youngs modulus	[N m^{-2}]
G	shear modulus	[N m^{-2}]
B	bulk modulus	[N m^{-2}]
ν	Poisson's ratio	[–]
ρ	density	[kg m^{-3}]
f	frequency of signal	[Hz]
λ	wavelength	[m]
Z_0	characteristic impedance	[MRayl]
T	transmission coefficient	[-]
Z_m	geometrical mean of two impedances	[MRayl]
R	reflection coefficient	[-]
H	height factor	[-]
A_g	amplitude of Gaussian function	[-]
A_p	amplitude of pressure signal	[-]
w_g	width of Gasussian function	[m]
w_p	length of pressure pulse	[m]
ld	distributed load discretization factor	[-]

1 Introduction

The objective of this master's thesis is to develop a numerical model that simulates the measurement of elastic waves within a solid domain generated by the photoacoustic (PA) effect. The model may facilitate the development of a novel forward-looking PA endoscope that integrates a relatively new PA imaging method for the first time. PA endoscopy is used for imaging the tissue layers up to several millimeters deep, with applications including intravascular imaging and imaging of the gastrointestinal tract. In Section 2.2, the requirements for PA endoscopy are presented. The most challenging requirement is achieving a frame rate exceeding 20 Hz while maintaining a reasonable resolution. Recently, novel imaging techniques, such as photoacoustic topography through an ergodic relay (PATER) [29], have been explored, based on a single sensor, which reduces complexity and speeds up frame rates. Further detailed information regarding PA endoscopy and PATER can be found in Chapter 2. This chapter provides a concise overview of the problem addressed in this master's thesis. The structure of the report is outlined at the end of this section.

1.1. PATER

Photoacoustic imaging (PAI) is a hybrid imaging modality using laser pulses to create ultrasound (US) waves from a material of interest. If the sources of the emerging US waves are known, an image can be constructed. PATER can perform this process with a simple right-angled glass prism and a single acoustic transducer. Frame rates of 2 kHz are reported by PATER while achieving a resolution of 5 µm [29]. PATER is thus a fast method, achieving a high resolution while being simple and robust. Further details regarding more traditional PA methods can be found in Section 2.2. This section will introduce the working principle of PATER.

Figure 1.1 shows a schematic representation of PATER. An acoustic cavity, in the form of a glass prism, is brought into contact with a sample. If PA signals are generated within the sample by a focused laser pulse, an initial pressure wave propagates through the sample and into the acoustic cavity. Within the acoustic cavity, the waves are reflected against the boundaries, and where the transducer is located, the reflections are measured. Due to the shape of the cavity and the location of the transducer, the measured signal is unique for every point in the field of view (FOV). The excitation area can be considered a pixel, although the size is not a direct measure of the resolution. With this focused excitation method, a calibration matrix can be constructed using signals from all pixels. For imaging, a wide-field excitation is employed, whereby the entire field of view is excited simultaneously. The signal, measured by the transducer in imaging mode, is a superposition of sets of signals coming from the individual pixels. A compressed sensing algorithm is capable of reconstructing which set of pixels were excited. This information can be used to generate an image.

The ability of this method to measure all the signals simultaneously without the need for a large number of small transducers, as done in other PA imaging methods, while still achieving a good resolution is an advantage over other methods.

1.2. A New PAE Design

Figure 1.2 presents an artist's impression of PATER within an endoscope. Currently, PATER uses a 15 mm large prism and a large needle transducer. Since the majority of forward-looking PAE endoscopes are constrained to a diameter of less than 4 mm [22], this setup is too large. Physically, it is relatively straightforward to miniaturize the PATER system. Right-angled prisms as small as 0.18 mm, 0.7 mm, 3 mm, and 5 mm can be purchased from suppliers. However, the needle transducer is incompatible with

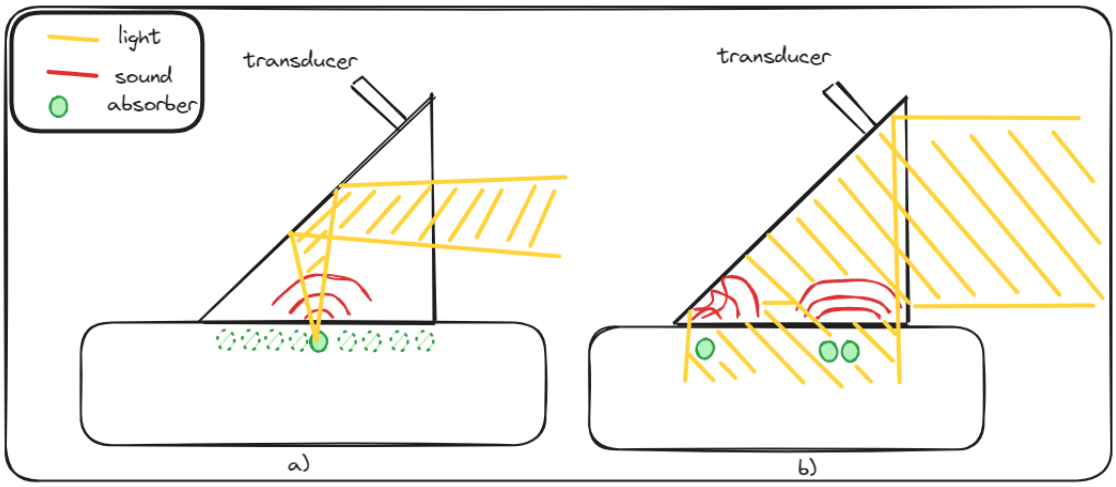

Figure 1.1: The working principle of PATER for two different modes is illustrated. **a)** The focused excitation mode or calibration mode. **b)** The wide field excitation mode or imaging mode.

an endoscope. An alternative approach is to use a piezo transducer affixed to the prism, analogous to the transducer from a method called photoacoustic computed tomography through an ergodic relay (PACTER) [47]. The size of such a piezo patch may need to be smaller than 1 mm; thus, the fabrication and handling of such a miniature piezo transducer will be challenging. Nevertheless, there are needle transducers on the market with piezo elements of 0.04 mm, 0.075 mm, 0.2 mm, and 0.5 mm, which indicates that this is a feasible approach. As the method is relatively novel, having been first introduced in 2020, there is currently limited knowledge regarding the design of an imaging system using PATER. Further research is required to fully understand the impact of miniaturization, the influence of body heat, the stresses from the housing, the sensitivity to a changing boundary after calibration, the cavity shape and the transducer on the performance of a PA endoscope design. Instead of performing only experimental studies, with all its challenges, a numerical model can help quantify performance parameters.

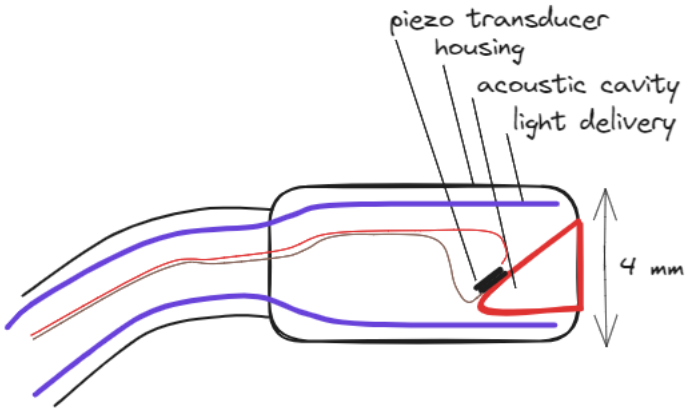

Figure 1.2: Artist's impression of a new forward-looking photoacoustic endoscope integrating a novel imaging technique called photoacoustic imaging through an ergodic relay (PATER).

1.3. Existing Models

Most publications concerning the numerical simulation of PA are related to the generation of PA signals. A recent article contains a good overview of the attempts up to this point and proposes a simpler mathematical model [42]. The methods in the publications vary, with the use of k-space and the finite element method (FEM). Multiple software packages are used, for example, k-wave and COMSOL.

K-wave is a software package based on the k-space method and designed for generating and propagating photoacoustic signals [52]. COMSOL is a multiphysics numerical software that allows the use of the boundary element method (BEM), the finite element method (FEM) and the discontinuous Galerkin FEM (DG-FEM) [49]. Some researchers have constructed more complex models, such as a photoacoustic resonator [26], or have integrated the generation and measurement of the initial wavefronts to simulate an imaging system [17], [20].

PATER and PAISE, evolutions of PATER [48], have been modelled in 3D using k-wave to compare their performances [48]. Unfortunately, the details of this study have not been published. Furthermore, it is essential to note that the simulation was conducted exclusively for longitudinal waves. Only simulating longitudinal waves is not a representative approach, as with many of the reflections additional wavefronts are generated due to mode conversion. The simulation is thus missing a large number of reflections, where the amount of missing reflections depends on the number of boundaries and simulation duration. Although not all of those reflections will be measured by the transducer due to the directional sensitivity, the choice of only simulating longitudinal waves can be questioned. Especially, since the researchers claim that more reflections enhance the resolution. A numerical model that describes a PA signal source and the representative measurement of its initial wavefront and reflections over time has yet to be reported for elastic waves.

1.4. Problem Definition

A new prototype of a PA endoscope is proposed that could enhance the performance of current state-of-the-art devices with respect to the frame rate and manufacturability. This new design involves the integration of a novel PA imaging method that is not understood very well yet. To facilitate the design of this novel PA endoscope a numerical model could be beneficial. Nevertheless, the modelling of this process is not straightforward due to the time dependency and high frequencies involved. Fortunately some parts of the process have been modelled already, which constrains the scope of this project. Figure 1.3 illustrates the process steps viewed from a physics perspective. This section will address the difficulties of modelling and state the objective of this thesis.

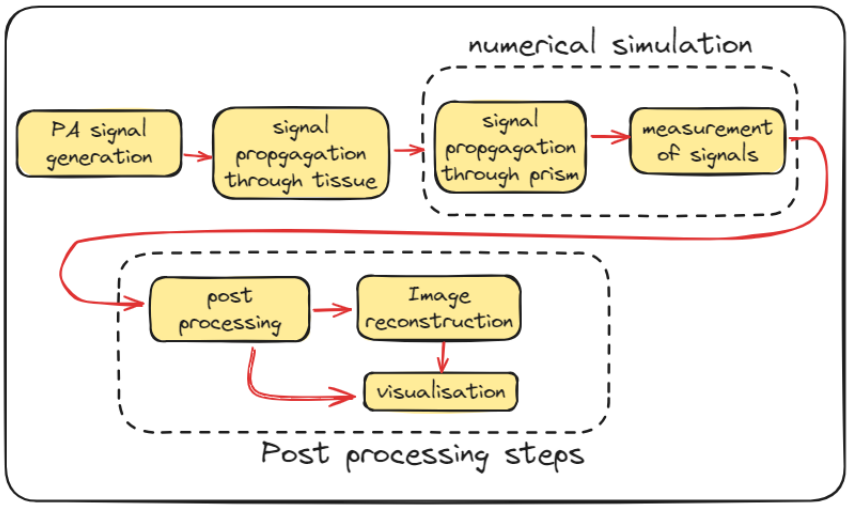

Figure 1.3: The general process steps of PATER is shown. Only a part of this process will be part of this project. The numerical simulation in COMSOL and the post processing with python and matlab.

Simulating the entire process, from the initial laser pulse to the final image, is difficult for three reasons. First, we have a proper multi-physics process, which begins with light propagation through tissue where diffusion and absorption occur. This is followed by transforming the absorbed light into heat and finally into an initial pressure wave by thermoelastic expansion. The initial pressure wave propagates through the tissue and refracts into the acoustic cavity. The waves subsequently propagate further with multiple reflections and mode conversions, depending on the boundary conditions of the prism, which are determined by the surrounding air, tissue and a transducer. At the end of this process, the displacement of molecules inside the piezo material is converted into an electrical signal. Simulating

the entire process, thus, results in a very complex model. Second, the PA signals operate in the MHz range, corresponding to short wavelengths. Those waves can only be resolved with a specific number of elements per wavelength. This results in many elements per domain and, thus, more degrees of freedom to solve for. Third, the simulation that is the subject of this study is time-dependent. The solver time steps of this time-dependent study are related to the element size and wave propagating speed. Smaller elements mean shorter time steps, resulting in longer calculation times. The multi-physics nature of the problem, the high number of small elements, and the short solver time steps combined make this type of simulation computationally costly.

The focus of this research project is on the propagation of the signals within the acoustic cavity and the measurement of those signals. Therefore, the PA signal generation and propagation through tissue is not part of this project. The decision to concentrate on these stages of the process was taken in order to simplify the simulation and because multiple models have already been published which focus on the signal generation. Although a k-wave model has been reported for a simulation of PATER, details have not been published. Furthermore, the model only simulates longitudinal waves. Consequently, there is still a gap in the modelling of such a process. Given the greater number of options available for the coupling of different types of physics, such as piezoelectric, heat and stress effects, this project has selected COMSOL to develop a model.

As discussed, the goal of the model is to aid the design of a new forward-looking PA endoscope. The different studies that could be designed would all need the same basis model containing at least a PA signal source, acoustic cavity, and method to measure the elastic waves within the cavity. COMSOL offers multiple options to extend or modify the model, but those models are out of scope for this project. The objective of this master's thesis can thus be formulated as follows:

> *Develop a numerical model in COMSOL that can simulate a photoacoustic imaging process comprised of an acoustic cavity and a single pixel sensor without the complicated PA signal generation*

The report structure is as follows: Chapter 2 provides background on PAE, PATER, PA signals, and acoustic waves. In Chapter 3, the design of the numerical model and all the important choices are discussed. The tuning, validation, and performance of the model are discussed in Chapter 4. Chapter 5 presents a discussion concerning the results. Finally, in Chapter 6, recommendations and future work are discussed.

2
Background

PA endoscopy can be divided into side-looking and forward-looking endoscopes, from which the forward-looking types especially have difficulties obtaining high frame rates. After a more detailed description of PAI is given in Section 2.1, the results of a literature study regarding forward-looking PA endoscopes is presented in Section 2.2. A brief state-of-the-art presentation of the recently explored new PAI techniques like PATER is given in Section 2.3. The basic theory behind the PA signal and its propagation as pressure and elastic waves is needed to achieve the objective of this project. Therefore, a short mathematical description of a PA signal is given in Section 2.4. The results of this section are used to generate an input signal for our model. Finally, in Section 2.5, an insight is given into elastic waves, where multiple wave types and boundary effects contribute to a complex system of waves and their behaviour.

2.1. Photoacoustic Imaging

PAI is a broad field with many different implementations. Even within photoacoustic endoscopy, multiple implementations exist. This section briefly explains PAI, the position of forward-looking PA endoscopes, and the properties of the current state-of-the-art PA endoscopes. For a more detailed explanation of PA imaging, many comprehensive review articles have been published [9], [12], [16], [21], [23]. Similarly for PA endoscopy [24], [27], [33], [34], [37], [43], [45].

PAI is a hybrid imaging modality using laser pulses to generate ultrasound (US) waves. By sending laser pulses, specific endogenous chromophores will absorb light depending on the wavelength. If the length of the laser pulse is within the thermal and elastic confinement region, the energy is converted into heat, leading to a thermal expansion followed by a contraction. This mechanism generates PA signals or pressure waves (in fluids and soft tissues). The PA signals can be detected by ultrasound sensors. With the time of flight known, the location of the PA signals is calculated, and an image is formed based on the absorption coefficient of materials in the field of view. Examples of endogenous chromophores and their absorption coefficients are given in Figure 2.1a. The timescale of a laser pulse is in the nanoscale range, and the wavelengths of light are in the visible and near-infrared part of the light spectrum. The frequency of the PA signals is generally in the megahertz range, and the amplitude is less than 10 kPa [9]. Instead of endogenous chromophores, it is also possible to use a contrast agent which extends the possibilities of PAI [9]. For an experimental setup, black rubber or ink are also suitable absorber materials.

The PA signals are generated almost immediately since the excitation pulses travel with the speed of light. If the speed of sound of the PA signals is known, the PA signal source can be located by measuring the arrival time. PAI can be used to obtain structural and functional information; a good example would be imaging the structure of a microvascular system, as can be seen in Figure 2.1b. By quantifying the concentration of specific chromophores via their spectral signatures, PAI can give functional information such as the blood oxygen saturation (sO_2) [9]. PAI has advantages over other modalities because of the depth of view, good resolution, and the information it can visualize.

Historically, there have been two main methods to obtain the origin of PA signals. There is photoacoustic computed tomography (PACT), where a wide-field light beam is exciting the sample and an array of acoustic sensors is used to measure the Pa signals. With a reconstruction algorithm based on back projection or phased array beam forming, an image can be formed [9]. The other method uses a focused excitation light beam and/or focused acoustic sensor and is called PA microscopy (PAM). For these methods, it is necessary to scan the full surface of the sample to obtain an image. The PACT

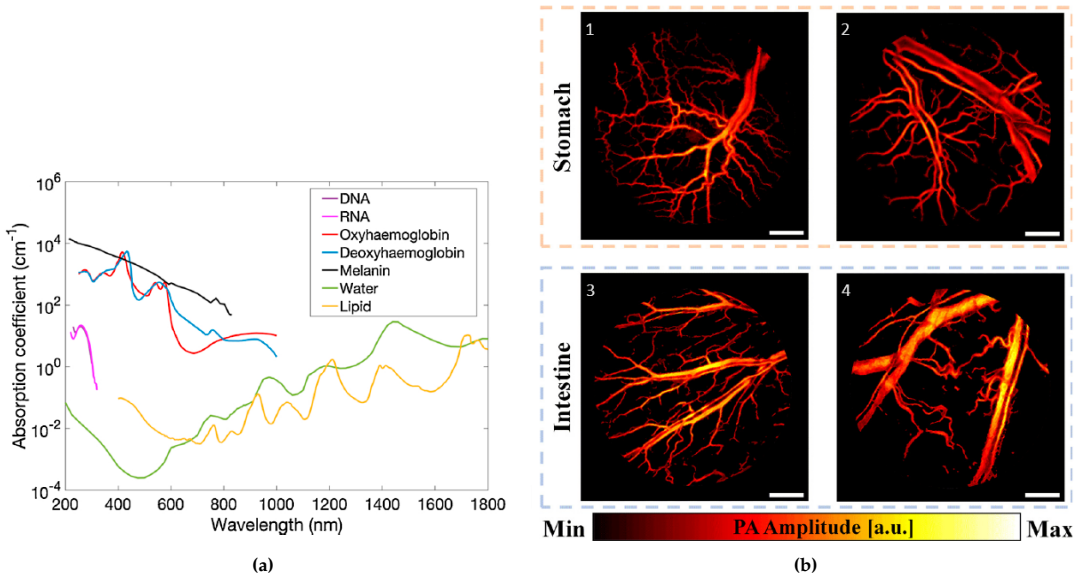

(a) (b)

Figure 2.1: a) Endogenous chromophores reproduced from [24]. **b)** PA maximum amplitude projection (MAP) images of the rat gastrointestinal wall. (1) and 2) Vasculature of the rat stomach wall. (3) and (4) Vasculature of the rat intestinal wall. The scale bars are 500 µm. Reproduced from [44]

methods are generally faster because they can measure all the PA signals simultaneously. PACT can also image deeper inside the body because PACT does not depend on a focused light beam. The disadvantage of PACT, especially for endoscopes, is the need for many small transducers. The advantage of PAM, in general, is the higher resolution it can obtain.

PA imaging can be used in four different implementations: as a tabletop, handheld, endoscopic, or in interventional systems. The field of PA endoscopes can be further divided into side-viewing and forward-viewing endoscopes. In this thesis, the PATER method is envisioned in a forward-viewing PA endoscope that can be used inside the working channel of a standard white light endoscope. The main reason for this focus is the low frame rates that this type of endoscope is able to achieve. The following section discusses the performance of the current state of the art.

2.2. Photoacoustic Endoscopy

Forward-viewing endoscopes are used in minimally invasive procedures for biopsy and procedural guidance such as in tumour biopsy, guidance of tumour removal, improve the guidance in foetal medicine (e.g. interventional procedures), and guiding needle biopsies [24], [25]. The forward viewing PA endoscope can be used inside the working channel (typically ~3.7mm in diameter) of a standard white light endoscope [22], integrated into a needle, or work as a stand-alone endoscope.

The main challenges involved in developing forward-viewing PAE probes are associated with integrating both the light delivery and US detection units within a miniature probe [24]. All forward-looking endoscopes integrate some sort of a scanning mechanism since building miniature transducer arrays is difficult and brings other challenges too, such as larger or more rigid probes.

Depending on the application, a set of requirements for the design of a PA endoscope can be obtained. This set comprises metrics such as size, flexibility, spatial resolution, depth of view (DOV), field of view (FOV), and frame rate. Some requirements must be met before the endoscope is suitable for clinical use. Naturally, the device should be easy to work with, but costs and robustness are also important. There are fabrication costs and operational costs. Operational costs are mainly due to decontamination and sterilization, and fabrication costs are primarily affected by the laser source, actuation mechanisms, and detection mechanisms [35]. The devices should also be robust so no damage occurs while in use or while cleaning [28]. Complex designs have more chance of failure, and more parts also lead to higher chances of failure. A specific part can fail due to multiple reasons, e.g. due to the exceeding of optical power or exceeding of the life cycle of a moving part. Fabrication errors can also lead to malfunctioning or earlier breakage of parts. Therefore, simple passive designs with fewer components are preferred.

Four groups are distinguished within the forward-looking PA endoscopes. References are given in Table 2.1. The first group comprises the endoscopes that use a scanning mechanism at the proximal end and a single-mode fiber (SMF) bundle to transport the light. The second group comprises endoscopes that use a rigid hollow tube to hold all the components and transport the light. The third group comprises, endoscopes using a digital mirror device or spatial light modulator and a multimode fiber to obtain a PA microscopy system. The Fourth and last group comprises endoscopes using a miniature scan mechanism inside the distal end.

In Figure 2.2, the variables are plotted in groups for a selected set of variables to illustrate the current state of the art. In the red area, the Fibre bundle (FB) based designs are shown; in the yellow area, the hollow tube (HT) designs; in the blue are the MMF-based designs; and in the green area, the designs with a scanning mechanism in the distal end. Some values seem to be zero, but those values are actually small and close to zero compared to the other values. The numbers in Figure 2.2 refer to the references in Table 2.1.

In Figure 2.2, two frame rates are given: a C-scan rate and a fast C-scan rate. The C-scan rate represents the system's frame rate containing the entire field of view. The fast C-scan rate is based on the pulse repetition rate (PRR) needed to obtain 20 Hz if possible at all. The PRR is limited due to aliasing, so for a larger depth of view the limit of the PRR is lower. To obtain a fast C-scan rate, very high pulse repetition rates are needed; see Appendix A for calculating the fast C-scan rate. High pulse repetition rates are required starting from 36 kHz up to 1540 kHz to obtain a frame rate of 20 Hz. These high pulse repetition rates are purely theoretical, and if a laser exists within the budget, the average power might be very high. In addition, the scan speeds also need to be able to follow this speed increase. A PA method like PATER that only requires a PRR of 2 kHz to obtain a C-scan rate of 20 Hz is therefore attractive.

Type	Ref.	nr
SMF + grin lens	[22]	0
SMF + hollow fibre	[18]	1
SMF + flexible PACT	[25]	2
SMF + rigid PACT	[19]	3
hollow tube	[32]	4
MMF 1	[41]	5
MMF 2	[40]	6
MMF 3	[30]	7
fibre scanner	[44]	8
MEMS scanner	[13]	9

Table 2.1: Table showing where the numbers in Figure 2.2 are referring to

2.3. PATER, PAISE, PACTER

A recently developed PA method using an acoustic cavity and a single transducer can reach frame rates into the kilohertz range. Beyond real-time imaging, this method opens up the ability to image fast dynamical processes. Examples are quantifying the stiffness of blood vessels via measuring pulse wave velocity, imaging of the responses of voltage or calcium indicators of neural activity, and high-speed clinical analysis of histological tissues [29]. In the published literature, the method is named PATER, PAISE, or PACTER [29], [47], [48]. All three differ in physical shape or algorithm used but are based on the same working principle. Compared to PACT and PAM, the method is much more straightforward in hardware, with only a single transducer and a solid acoustic cavity.

Starting with PATER, or photoacoustic topography through an ergodic relay [29]. The ergodic relay (ER), a right-angled glass prism, guides incoming waves at any point from the input surface to any point on the other surfaces. This is possible because of the ergodic properties of the prism. In other words, the shape of the prism is such that every incoming wave will reflect in a way that it will eventually reach all points in the prism. Provided the ER is designed correctly, the reflections are unique for every source location. These temporal signals can be measured in parallel using only a single transducer. In the next step, the temporal signal can be decoded to reconstruct an image. The decoding uses a two-step iterative shrinkage thresholding (TWIST) algorithm [6]. Impulse responses from the entire FOV are

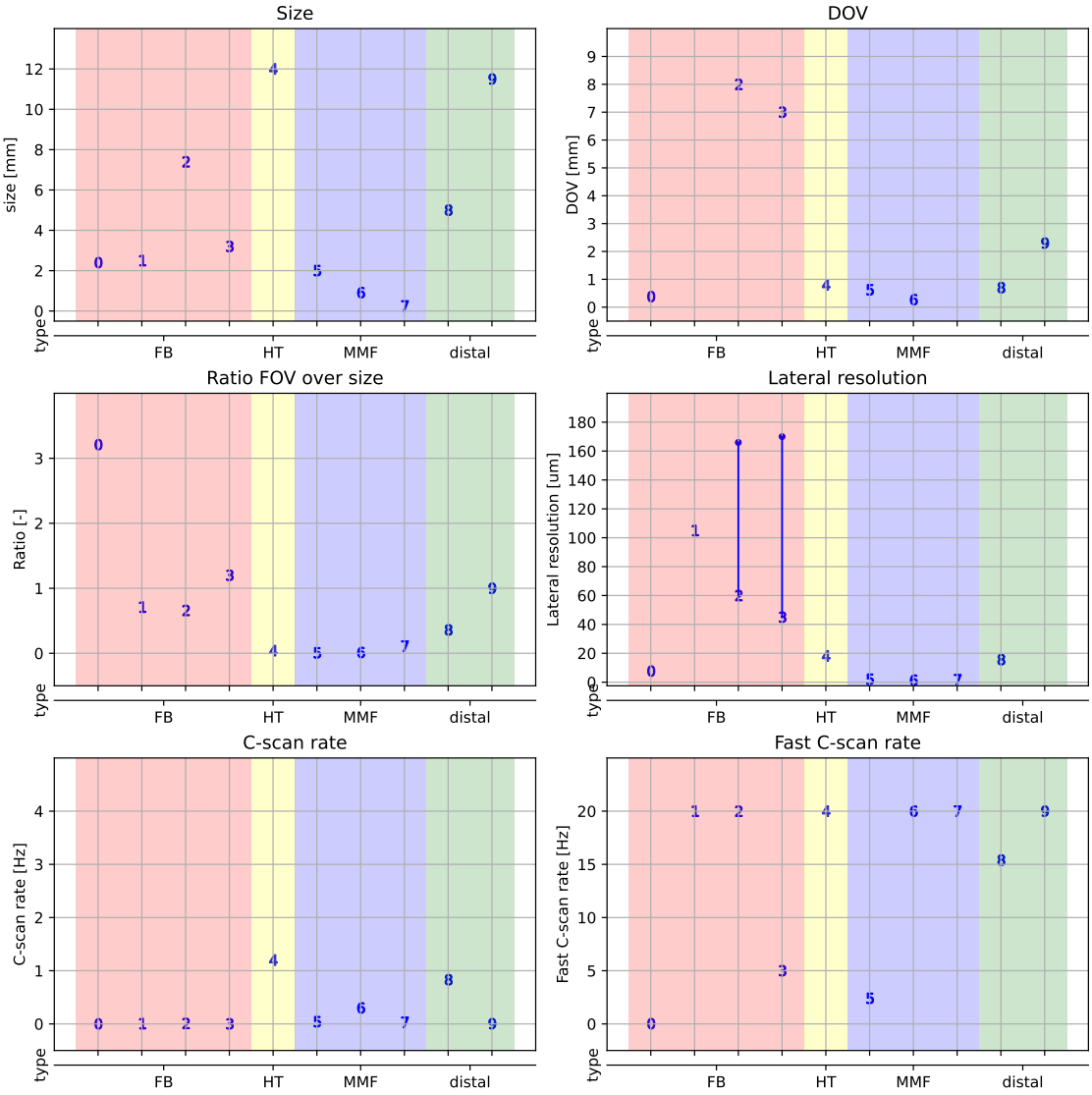

Figure 2.2: Performance of State of the art forward looking photoacoustic endoscopes. Divided in 4 groups, FB: fibre bundle based methods, HT: hollow tube based method, MMF: multimode fibre based methods, distal stand for scanning mechanisms in the distal end.

collected in a focused excitation mode to calibrate the prism. This set of impulse responses can be used to reconstruct the image from the signals measured in wide-field excitation mode. The authors showed 2D images resulting from 2D calibration and mentioned the option of 3D calibration for 3D imaging. The boundary conditions of the ER influence the reflections. Because the boundary conditions change if the ER is in contact with an object, the reflections also change. A new calibration is, therefore, needed for every object. Calibrations are time-consuming, and a scanning mechanism is required. Calibration for every object, thus, limits the practical implementation of PATER.

A new acoustic cavity shape was reported such that only one calibration is needed for different objects [48]. This shape consists of the same right-angled prism but now with a slender rod on top. The rod acts as a waveguide between the object and the prism. Measured reflections via the surface of the waveguide in contact with the object will still be different for each object. However, the rod acts as a delay, so there is a time window when measurements can be done without object-specific calibration. Researchers named this configuration PA imaging through a spatio-temporal encoder (PAISE). To create 3D images, a 3D calibration should be performed; another group has reported such experiments using a similar set-up as PAISE, calling it SS3D-PAI [46].

Recently, an article using the same acoustic cavity as PAISE but with a different transducer has 3D

capabilities without 3D calibration [47]. The authors called their method PACT through an ergodic relay (PACTER). In contrast with PAISE, they claimed to have made 3D images. PATER and PAISE used a needle transducer to measure the signals, whereas PACTER uses a homemade piezo element glued on the cavity. PACTER also makes use of a different reconstruction algorithm. PAISE and PATER using a TWIST algorithm and PACTER, a self-developed algorithm in combination with a fast iterative shrinkage thresholding algorithm (FISTA) for linear inverse problems [7], [47]. The self-developed algorithm enabled 3D imaging with a 2D calibration step using the acoustic cavity surface points as virtual transducers.

The two configurations are shown in Figure 2.3.

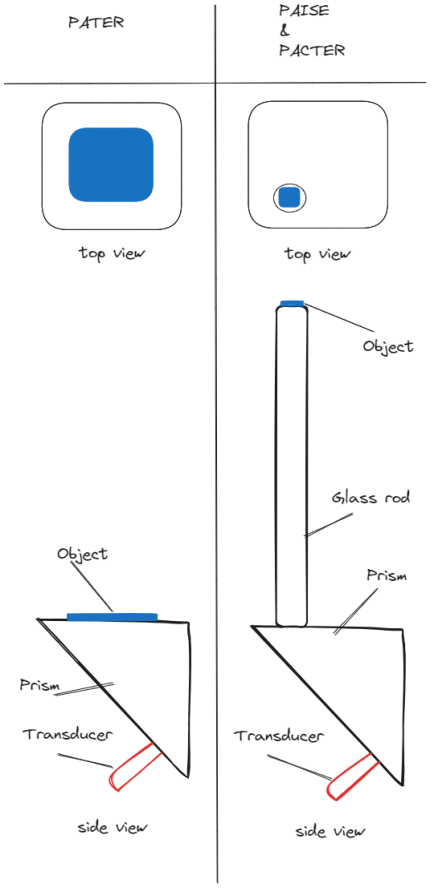

Figure 2.3: The PATER, PAISE, and PACTER configurations are shown from the side and top. The main difference is the glass rod, which acts as a delay function for the signals and, as such, allows for imaging without object-specific calibration. In addition, PACTER does not use a needle transducer but a piezo patch affixed to the prism.

2.4. The Photoacoustic Equation

A photoacoustic signal (PA) is generated by the excitation of a sample with a laser pulse. The mathematical models describing the generation of a PA signal can be complicated. For our model, we need an input signal representative of a PA signal, and in this section, options for our model are discussed.

A detailed derivation of the PA equation is given in [9], [11], [38]. Here, we only show the result of this derivation. The photoacoustic equation is given in 2.1

$$\left(\nabla^2 - \frac{1}{c^2}\frac{\partial^2}{\partial t^2}\right) p(\mathbf{r}, t) = -\frac{\beta}{C_p}\frac{\partial H}{\partial t} \tag{2.1}$$

Where p is the pressure at position $\mathbf{r}$ and at time t, c is the speed of sound, β the thermal coefficient of volume expansion, C_p specific heat capacity at constant pressure, and H the heating function. The

heating function is defined as the amount of thermal energy converted per unit volume and per unit time.

$$H = \eta \mu_a \Phi \tag{2.2}$$

Φ is the optical fluence rate, η is the percentage of optical energy converted into heat, and μ_a is the optical absorption coefficient.

In literature, solutions are reported for specific cases. Delta-pulse excitation and finite duration excitation for a slab and sphere are discussed [11]. Others have obtained the response solutions of different geometrical shapes for fluids and solids to gain knowledge about the properties of the response [1], [3], [4], [39]. A typical N-shaped PA signal coming from a sphere is shown in Figure 2.4 taken from [3].

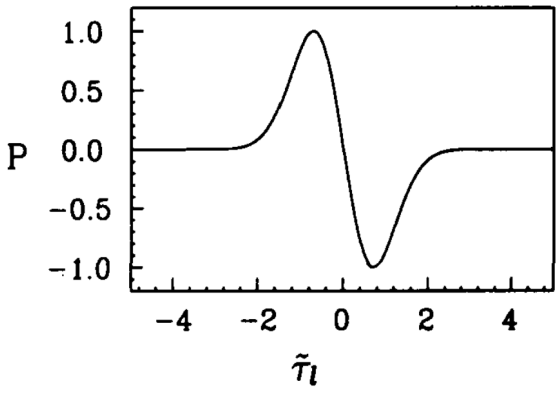

Figure 2.4: A typical PA signal from a excited sphere, reproduced from [3], with pressure P in arbitrary units and $\tilde{\tau}_l$ a dimensionless time

An important conclusion for this project is that the PA signal from a small spherical object is proportional to the derivative of the excitation pulse . If we assume a Gaussian excitation pulse in time, a PA signal is thus proportional to the derivative of a Gaussian function. The width of the Gaussian function is defined as the length of a laser pulse and the amplitude as the peak power [11].

2.5. Acoustic Waves

In general, there are three wave types occurring in fluids (including gases) and solids: longitudinal waves, transverse waves and Rayleigh waves. Appendix B briefly explains the different types. Longitudinal waves in fluids are also called pressure waves, and the waves occurring in solids are referred to as elastic waves. For building and examining the model, the essential properties and behaviour of the specific waves in the domain must be known. This section gives values for the speed of sound and wavelength in different media, as well as transmission and reflection coefficients for normal incidence in a fluid-fluid interaction. A typical elastic wave phenomenon, called mode conversion, happening at the interface between combinations of solids and fluids, is briefly discussed. Finally, the mechanisms that cause the loss of signal strength over time are discussed.

Each wave has its propagation speed and can be calculated for the different waves according to [2].The wavelength of the waves is due to the different speeds also different and can be calculated with Equation

c_p	$\mathrm{m\,s^{-1}}$	longitudinal fluid wave speed	$c_p = \sqrt{\frac{B}{\rho}}$ (2.3)
c_1	$\mathrm{m\,s^{-1}}$	longitudinal wave speed	$c_1 = \sqrt{\frac{E(1-\nu)}{\rho(1+\nu)(1-2\nu)}}$ (2.4)
c_2	$\mathrm{m\,s^{-1}}$	transverse wave speed	$c_2 = \sqrt{\frac{G}{\rho}}$ (2.5)
c_R	$\mathrm{m\,s^{-1}}$	rayleigh wave speed	$c_R = 0.9194 c_2$ (2.6)
E	$\mathrm{N\,m^{-2}}$	youngs modulus	$\lambda = \frac{c}{f}$ (2.7)
G	$\mathrm{N\,m^{-2}}$	shear modulus	
B	$\mathrm{N\,m^{-2}}$	bulk modulus	
ν	–	Poisson's ratio	
ρ	$\mathrm{kg\,m^{-3}}$	density	
f	Hz	frequency of signal	
λ	m	wavelength	

2.7.

Where $c1 > c2 > cR$. The speed of sound and wavelength for different waves and media are given in Table 2.2. The wavelength is calculated for a frequency of 20 MHz equal to the upper limit of the frequency bandwidth of the signal used in this thesis.

2.5.1. Reflection, Refraction, Impedance

Whenever there are material changes waves are reflected and refracted. Both the reflected and refracted waves are altered due to this phenomena. In this section we will describe the effects of reflection, refraction on the waves. In this explanation impedance will also be discussed.

Typical reflections and refractions can be seen in Figure 2.5.

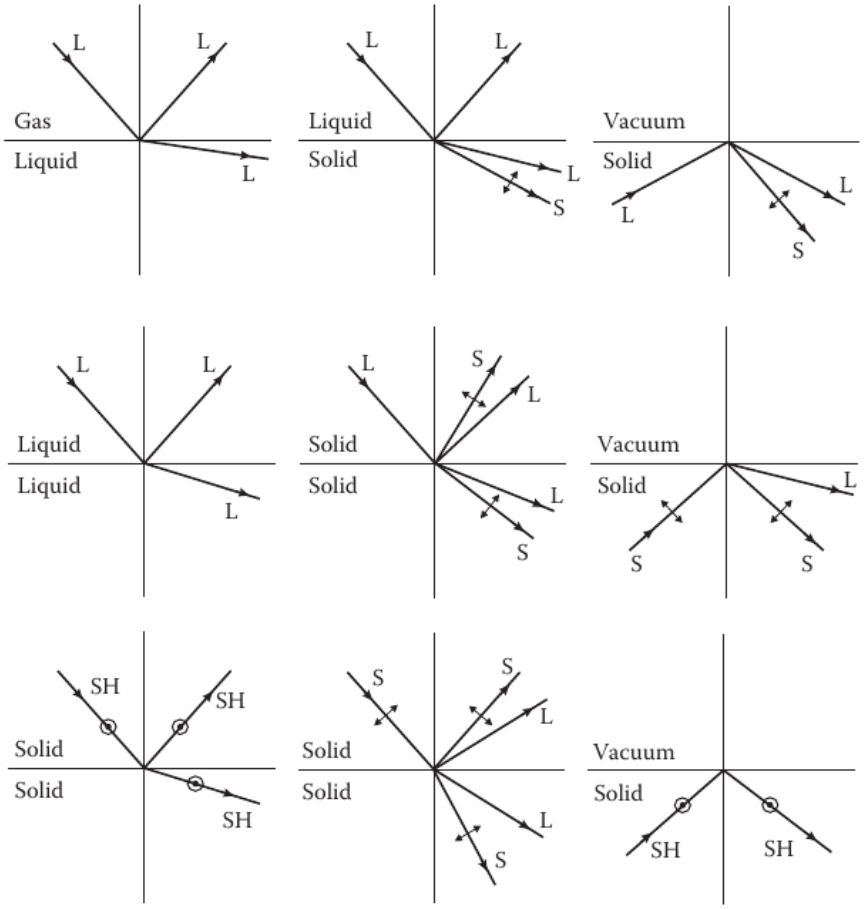

Figure 2.5: Typical cases of reflection and transmission of acoustic waves at interfaces between solids, liquids, and gases. L stands for longitudinal waves, S(V) for vertically polarized transverse waves, and SH for horizontally polarized transverse waves. Where Horizontal is out of plane in a 2D situation [10].

Interestingly, with every refraction and reflection, an extra wavefront emerges in our acoustic cavity, with the exception of incoming horizontally polarized shear waves.

We are interested in the reflection and transmission coefficients to quantify the loss of signal when PA signals enter the prism from a tissue-like material, when elastic waves in the prism reflect at the plane in contact with the tissue-like material, when elastic waves reflect at the planes in contact with air, and when elastic waves reflect at boundary parts that are in contact with the housing holding the prism.

To approximate the transmission and reflection coefficients, we can calculate this for a normal incidence case of a fluid-fluid interaction [10]. It is also possible to define this for other combinations and different angles, but that would make things more complicated than necessary for this project. The characteristic impedance (Z_0), transmission coefficient (T), and reflection coefficient (R) can be calculated by [10]

$$Z_0 = \rho c_1 \tag{2.8}$$

$$T = \frac{2Z_2}{Z_1 + Z_2} \tag{2.9}$$

$$R = \frac{Z_2 - Z_1}{Z_1 + Z_2} \tag{2.10}$$

$$T = R_p + 1 \tag{2.11}$$

Where Z_1 and Z_2 are the characteristic impedances of the two media at a boundary.

		glass	air	water	polycarbonate	aluminium	PZT-5H
c_1	[m s^{-1}]	5972	343	1485	2061	6197	4580
c_2	[m s^{-1}]	3765	-	-	841	3121	-
c_R	[m s^{-1}]	3462	-	-	773	2870	-
λ_{c1}(20 MHz)	[µm]	298	17	74	103	310	229
λ_{c2}(20 MHz)	[µm]	188	-	-	42	156	-
λ_{cR}(20 MHz)	[µm]	173	-	-	39	144	-
ρ	[kg m^{-3}]	2203	1.16	997	1200	2700	7500
Z_0	[MRayls]	13	4e-4	1.5	2.5	17	34

Table 2.2: Material properties of glass, air, water, and polycarbonate. Also the speed of sound and wavelength for the different wave types is presented.

	air	water	polycarbonate	aluminium
T	6e-5	0.20	0.32	0.88
R	0.9999	0.80	0.68	0.12

Table 2.3: Transmission coefficients of glass combined with: air, water, polycarbonate and aluminium. Calculated for a normal incidence on a fluid-fluid interface.

2.5.2. Signal Loss

A loss of signal in the period between entering the prism and the measurement can be explained by three mechanisms. First, we have spreading due to the circular/spherial propagation of the wave fronts. Second, there is mechanical damping related to the travel distance. And third, there is transmission to other domains. How much energy is lost to different domains is depending on the transmission coefficient and the domain of interest, as defined in 2.5.1.

Mechanical losses can be described by Rayleigh damping

The pressure in cylindrical/circular waves proportional to $\frac{1}{\sqrt{r}}$ and for spherical waves this is $\frac{1}{r}$ [5]. This difference is important for our validation simulation, where we compare a 2D simulation with 3D experimental results.

Due to the large range of the acoustic amplitudes a logaritmic scale is often used. The sound pressure level (SPL) is often used and defined as:

$$SPL = 20 \log \left(\frac{P}{P_{ref}} \right) \tag{2.12}$$

Or when calculating the difference of two sound levels:

$$SPL = 20 \log \left(\frac{P_1}{P_2} \right) \tag{2.13}$$

In this report we will use 1 µPa as reference level [5].

2.6. Summary

This chapter started by discussing the state-of-the-art, forward-looking PA endoscopes. The literature study found that they all have too low frame rates or that their manufacturability is low.

We discussed the state-of-the-art PA methods using an acoustic cavity and single transducer. The conclusion is that the PATER method is, due to its larger FOV with respect to the overall size, a better choice compared to PAISE and PACTER. There are three essential downsides: PATER has to perform object-specific calibration, the size is incompatible with the size requirements of PA endoscopes, and the current transducer is too large. Looking at the other two publications, PAISE and PACTER, we can combine solutions from all of them to create a solution for an endoscope. The first challenge in getting PATER to work inside an endoscope is the transducer design in combination with a small acoustic cavity. The second challenge is the ability of this combination to perform a calibration outside the body that is still valid for particular areas in the body.

We explored the nature of PA signals and the current analytical approaches to obtain solutions for simple objects. Those methods are complicated and not easy to tune the way we want.

We also provided an overview of the different waves in fluids and solids and the formulas to derive their main properties, such as wave speed, wavelength, transmission coefficients, and reflection coefficients. This information is invaluable in understanding the principles behind elastic wave behaviour.

3
Method

This chapter gives a description of the model developed as part of this thesis for simulating an acoustic cavity for single-pixel photoacoustic imaging. The model will be described and tested in 2D, as a 3D model proved to be computationally costly (see Section 4.6 for a comparison of 2D and 3D models). If needed, the model can easily be transformed into a 3D using the same strategy. Figure 3.1 shows an illustration for all parts of the model.

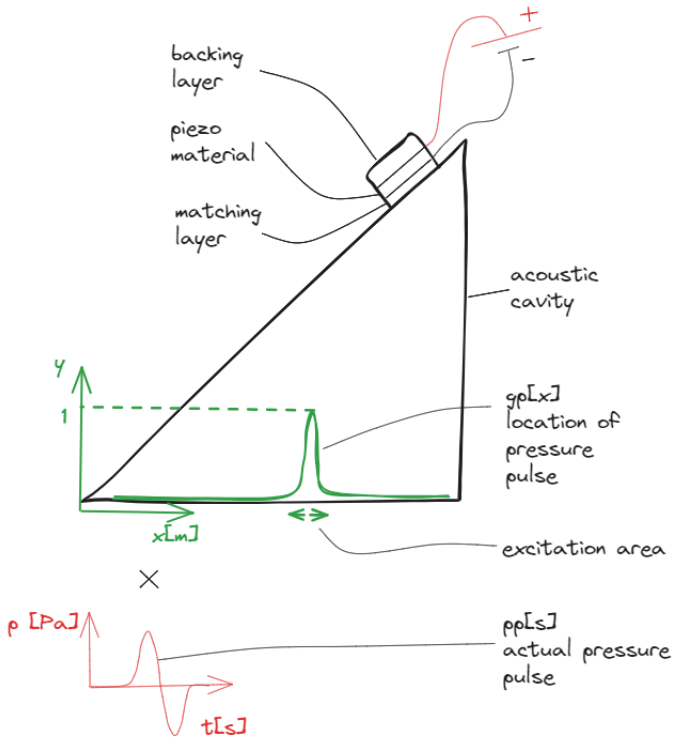

Figure 3.1: The COMSOL model with all the important parts is illustrated in 2D. The Gaussian function, gp(x), and the pressure pulse, pp(t), multiplied together define the load distribution on the imaging plane.

The model comprises of a solid domain that represents a section of a right angled prism, an impedance matching layer, a piezo material layer, and a backing layer. The incoming PA signals are defined as a distributed boundary load normal to the imaging edge. The boundary load itself is a combination of a Gaussian pulse (gp(X)) that defines the spatial amplitude of a PA signal and a pressure pulse (pp(t)) represents the pressure over time.

The pressure pulse is discussed in 3.1, and the parts defined using COMSOL are discussed in 3.2. The most important decisions to set up the COMSOL model are discussed there.

3.1. Input Signal

The main characteristics of a PA signal are the typical N shape, the amplitude A, and the length w. In this section, a representative signal is formulated to generate the typical N-shaped pulse with a specific

amplitude and length. The amplitude represents the signal strength, and the length determines the signal's frequency content. Suppose a signal is used where the frequency content can be tuned such that it is equal to the upper limit of the used transducer in an experiment. In that case, the results between a numerical simulation and a lab experiment should be equal. Such a tunable signal eliminates the need to simulate a very high frequency that is not measured anyway. The goal is thus to obtain a function that can generate a PA signal with a specific amplitude and frequency content.

In Section 2.4, we stated that the derivative of a Gaussian function is proportional to an actual PA signal coming from a small sphere. This understanding led to a function based on the derivative of a Gaussian function with a tunable amplitude A_p and length w_p. The length is measured at a certain height relative to the amplitude and this height can be defined as $\frac{A_p}{H}$. An illustration of the w_p value at a specific height is given in Figure 3.6a. The standard derivative of a Gaussian function is normalised to obtain a tunable function so a variable can be used to determine the amplitude. In addition, a factor was added to change the variable for the length so that this variable actually represents a meaningful length. See Appendix C for a complete derivation. The formula for the pressure signal is given by Formula 3.1.

$$pp(x) = A_p \cdot e^{\frac{1}{2}\left(\frac{2\sqrt{2ln(H)}}{0.8w_p}\right)(t-t_0)} \cdot e^{\frac{-1}{2}\left(\frac{2\sqrt{2ln(H)}(t-t_0)}{0.8w_p}\right)^2} \tag{3.1}$$

We can plot a graph showing the center frequency, and upper limit of the the frequency spectra of PA signals with different lengths; see Figure 3.2a. The transducer used to generate the experimental data our model is compared to has an upper limit of 20 MHz. We thus choose a signal length of 225 ns, see Figure 3.3. The frequency of this signal is plotted in Figure 3.2b.

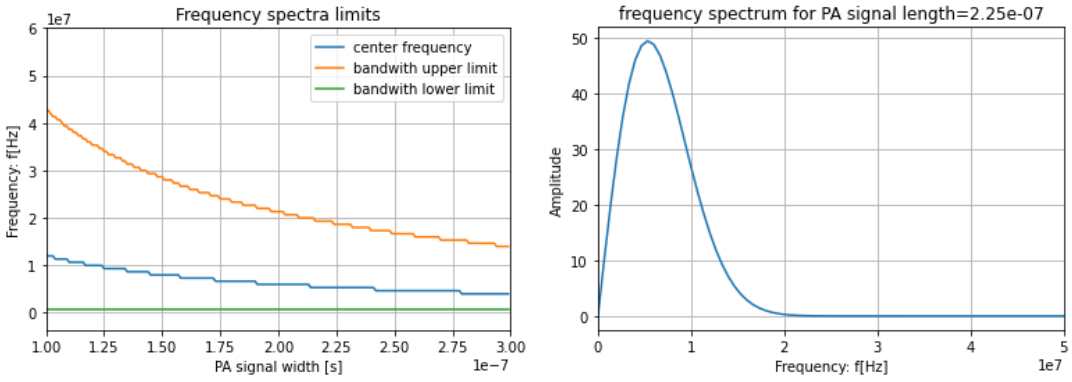

(a) (b)

Figure 3.2: a) A graph showing the frequency limits and center frequency for different PA signal lengths. **b)** The frequency spectrum of a PA signal with a length of 225 ns.

3.2. COMSOL Model

The COMSOL model is a 2D geometry comprising an acoustic cavity and a piezo transducer. The PA signals are introduced as a load distribution onto the imaging plane of the acoustic cavity. The model is designed like this for multiple reasons. First, omitting a layer containing the absorber structures, like a layer of tissue, makes the model more straightforward and, thus, a better starting point. Second, most of the experimental tests at the beginning of the lab experiments contain a test where a thin absorber is glued or painted on the acoustic cavity. The latter is the case for experimental data from the research group that published PATER [36]. Constructing a similar model allows for calibration with this data. In Figure 3.1, an illustration is given of the model.

COMSOL has built-in multiple numerical methods to solve problems. A time-dependent method is used since we are interested in the transient part of the response to a PA signal. Precisely, a method based on the discontinuous-Galerkin FEM (DG-FEM). This method is more memory efficient than a standard FEM and should perform well on a cluster due to the local nature of the method. Within COMSOL, there is the option to simulate elastic waves and pressure waves. The interfaces differ but can

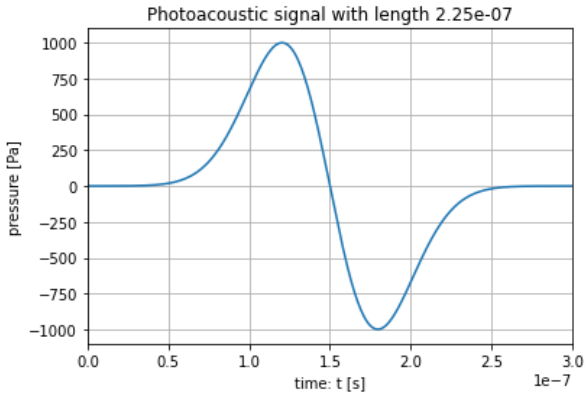

Figure 3.3: The PA signal having a length of 225 ns and containing frequencies up to 20 MHz

be coupled to obtain a vibro-acoustics model. In addition, an electrostatic interface can be coupled such that a piezo transducer can be simulated.

3.2.1. Boundary Load

As done in a seismic sample from the COMSOL examples [50], a distributed load is defined by a Gaussian function, gp(x), multiplied by a 1D pressure signal, pp(t). The Gaussian function has a maximum amplitude of 1 and is given by equation 3.2. This solution defines a spatial and temporal pressure load value over a line or surface. An illustration can be seen in Figure 3.1. Using this method, we have complete control over the location of the pressure pulse and spot size. Where the spot size is taken as the FWHM of the Gaussian function, if multiple Gaussian functions are added together, we can also define an image containing multiple pixels. Both the calibration mode and imaging mode can thus be simulated.

$$pp(x) = A_g \cdot e^{\frac{-1}{2}\left(\frac{2\sqrt{2ln(H)}(x-x_0)}{w_g}\right)^2} \tag{3.2}$$

3.2.2. The Mesh

The size of the mesh is important for the quality of our solution. A smaller mesh size generally leads to better solutions but larger files and computation times. Therefore, a mesh convergence study to find the largest mesh size is important to obtain a solution within a specific error and optimise for memory and computation time. In a static case, the number of elements is directly related to the computation time, and the size of individual elements is unimportant. For a time-dependent study, the solver step time is an additional variable that influences the computation time. The solver step time is directly related to the 'cell time scale'. The 'cell time scale' is calculated with the fastest wave and the smallest element in a domain. The size of the smallest individual element is thus important for the computation time in a time-dependent study. In Chapter 4, the results of a mesh convergence study are discussed; here, the mechanisms determining the mesh size and the methods used to build our mesh are discussed.

Three mechanisms in our simulation determine the mesh size. The first is the dimension of features in the domain, such as the thin matching layer of the transducer. Second, the number of elements per wavelength is important to resolve specific frequencies. Third, a distributed load must be adequately discretised to ensure all energy is converted into the mesh nodes. Figure 3.4 shows the different regions of interest

To avoid unnecessary small elements, geometric features that are small and estimated to be of low importance should be omitted. Thin layers of acoustic gel and small fillets and chamfers are thus omitted.

The maximum size of the elements is further restricted by the number of elements per wavelength (epw), calculated with Equation 3.4. According to COMSOL, DG-FEM performs best when using 4th-order elements and 1.5 up to 2 elements per wavelength [51]. If the Nyquist sample theorem approximates the number of elements per wavelength, a value of 2 is advised independent of the

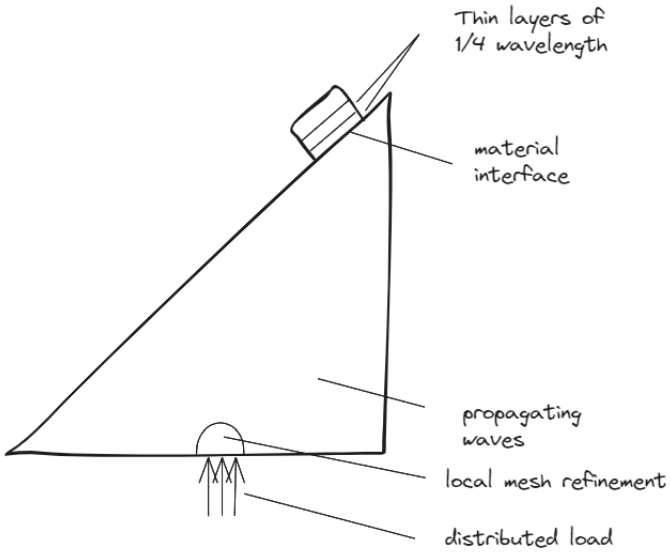

Figure 3.4: The model has specific areas of interest for adequate meshing.

wavelength used. See Appendix D for more information on the calculation. The maximum element size for silica glass, aluminium, PZT-5H, air, and water are shown in Figure 3.5 for different values for epw. Since the wavelength depends on the speed of sound of a particular domain, the element size differs per material.

COMSOL offers two methods of meshing for domain boundaries with different element sizes: a conforming mesh and a non-conforming mesh. When a conforming mesh is used, the element size around the boundary conforms to the other element size. This results in smaller elements than needed in the material with the higher speed of sound, leading to smaller solver time steps. On the other side of the boundary, the larger elements cause a lower accuracy due to fewer elements per wavelength. The non-conforming mesh option, which connects to domains with a continuity condition without conforming the mesh, is a preferable alternative. However, it's not without risks, as unstable models have been encountered inside thin transducer layers. More research is needed to determine the requirements for using this option.

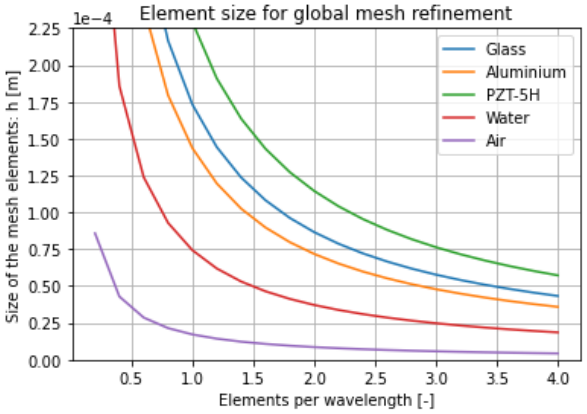

Figure 3.5: The mesh element size can be calculated for the slowest wave in the medium for different materials and different values of elements per wavelength (epw).

$$\lambda_{min} = \frac{min(c_1, c_2, c_R)}{f} \tag{3.3}$$

$$hmax = \frac{\lambda_{min}}{epw} \tag{3.4}$$

The load distribution is given by the width of a Gaussian distribution on one of the prism's edges. The targeted resolution is in the tens of millimeter range, while the element size for glass would be around a 100 µm. A fast-changing load value, like our steep Gaussian curve, causes problems when converting all the energy of the load to the nodes. The Nyquist sampling theorem approximates how many nodes are needed to sample the load correctly. A mesh convergence study is performed in Chapter 4 to prove a valid mesh refinement.

For the mesh refinement of the Gaussian load distribution, the Nyquist sample theorem approximates the node distance of the elements; see Figure 3.6a for a visualization of the mesh refinement. Since we are using fourth-order elements, one edge of each element can be divided by four to obtain an approximation of the node distance. This distance is compared with the sample distance obtained using the Nyquist sample theorem. To get a more general result, the FWHM of the Gaussian function is dicretized instead of a specific value of the width. This can be done by specifying a value ld for the number of elements over a distance equal to the FWHM.

The Nyquist sampling theorem for a FWHM of 50 µm results in a maximum sample distance of 25 µm. This equals an element size of $\frac{FWHM}{ld}$ where ld is 0.5. The length of the mesh refinement line is twice the Gaussian function's base width. A mesh refinement study is performed by varying the value of ld. For more details regarding the result of the Nyquist sampling theorem, see Appendix D.

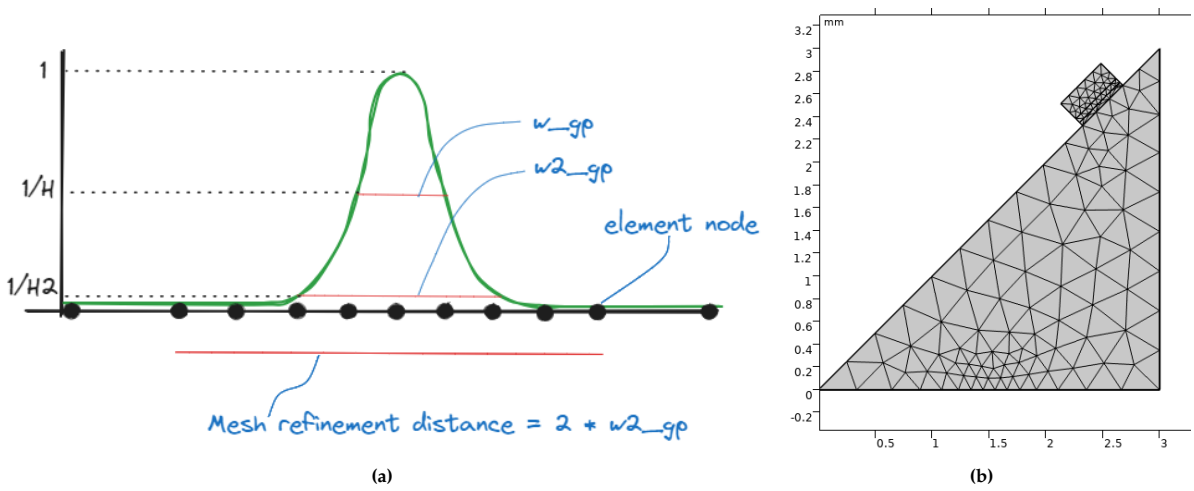

(a) (b)

Figure 3.6: a) The discretization of the load distribution visualized. **b)** The result is shown for a coarse conforming mesh of 0.47 epw.

The meshing strategy is thus to set the maximum and minimum size of the elements equal to a certain amount of elements per wavelength, omit small geometric features, and use local mesh refinement for the discretization of the load distribution. The non-conforming mesh has the risk of being unstable and is not used. In addition, for this case, the time steps of the solver are defined by the size of the local mesh refinement of the load area and not by small elements introduced due to a conforming mesh.

3.2.3. Boundary Conditions

The edges of our model are standard modelled as a 'free boundary', meaning no constraints or forces are acting on this boundary. There are two additional conditions specified. The outer surface of the backing layer is set to be a low reflecting boundary; this means that COMSOL attempts to create a perfect impedance match with the outside world. In reality, a backing layer is designed with a high mechanical damping, which causes the signal to be absorbed as much as possible. We did not create a proper backing layer for our simulations and simulated its behaviour with the low reflecting boundary

condition. The other boundary condition is the distributed pressure load described earlier. This load effectively defines a zero pressure condition after the pressure pulse, which behaves like a reflecting boundary. In reality, large parts of the edges are in contact with air, but we omit the whole air domain since the transmission coefficient is almost zero, as calculated in Table 2.3. In Section 4, we show that the measured signal does not change if air is omitted.

3.2.4. Measurement of Elastic Waves

An accurate measurement method is needed to obtain meaningful results. Within COMSOL, multiple options are available to simulate a measurement of the elastic waves inside a domain. Since designing a full transducer model is outside the scope of this project, a brief effort is made to model a simple transducer without tuning for a specific center frequency, bandwidth, directionality, and sensitivity. The goal of this model is to show the potential of such a transducer model and to compare it with the second method used. This second method is used for most of the results and is a simple line average over the transducer surface. The normal component of traction is used as a variable since the electric current is proportional to the stress in the piezoelectric material.

In a later version of PATER, PACTER, a piezo patch is designed for the measurements. For this model, the same architecture is used, which was chosen by the researchers of PACTER for optimal sensitivity and transmissibility [47]. The transducer model comprises three layers fixed to the surface of the acoustic cavity: an impedance-matching layer, a piezo material layer, and a backing layer where signals should be absorbed. The main variables of the transducer design are the dimensions of the three layers and the material types.

For the piezo material, we have chosen PZT-5H; it is a sensitive material and is available in COMSOL. The matching layer impedance should equal the geometrical mean, Z_m, of the acoustic cavity impedance and piezo material impedance to obtain the maximum transmission. Z_m is defined in Equation 3.5 [8], [10], [31].

$$Z_m = \sqrt{Z_1 Z_2} \tag{3.5}$$

The acoustic transmission from glass to PZT5H is thus maximum when the matching layer has a characteristic impedance of 21 MRayl. There are models to engineer an optimal epoxy-filled composite [8], but this was out of scope for this project. Instead, we used aluminium with a characteristic impedance of 17; see Table 2.2. The layer thickness of the matching layer was taken as a multiple of a $\frac{1}{4}$ wavelength of the center frequency; this is a good starting point according to literature [8].

For reasonable transmission into the backing layer, also aluminium was used for this layer. The thickness was chosen arbitrary and a low reflecting boundary layer was used to simulate the absorption of wave energy.

3.3. Cluster Computation

As discussed in the intro, the computations can quickly become heavy for the type of simulations performed. Fortunately, COMSOL supports the use of clusters, where the simulation can be divided into multiple cores for both shared and distributed memory configurations. Unfortunately, COMSOL is not reported to be very good at parallelization. The DG-FEM method should be very suited for parallelization if the computation time scales well with the increase of cores. Larger models or models with higher frequencies can be simulated more easily.

In Delft, a cluster called DelftBlue is available, and master students are allowed to use it but with the restriction of 24h simulation time and a maximum of 48 cores. In this thesis, a small script is written that allows running COMSOL on DelftBlue. The script is simple, but because the information to build it is spread over multiple sources, it is mentioned in this section. The script can be used for single simulations and parametric sweeps. The settings are such that all the large files, e.g. recovery files, are stored in a location of preference, preferably on a shared memory location. The script is easily changed for any other cluster and can be found in Appendix G.

3.4. Summary

A simple and modular COMSOL model is constructed to simulate the measurement of Pa signals within an acoustic cavity. DG-FEM is used because it is known for its memory efficiency and scalability on

clusters. A simple and tunable PA signal is defined as an input signal of the model. If needed, this signal can easily be replaced by a more case-specific signal due to the combination of a pressure pulse and Gaussian function to define a boundary load. The COMSOL model is built with only the strictly necessary domains to keep the computational costs low, and the mesh size is kept as large as possible to avoid long computation times. Currently, a basic transducer model has been added to the COMSOL model to show the potential of this model. However, designing and tuning this transducer was not part of the scope of this project; the transducer model is thus not optimal. The model can be used to investigate the behaviour of PATER and other shapes of the acoustic cavity and design a suitable transducer. Since COMSOL has multiple options to add other physics modules, the model can easily be modified to suit different research questions.

4
Results

In this chapter, the model is tuned, tested and validated against lab experiments. In Section 4.1, the results of two mesh convergence studies are discussed. The results of this study are used in all following studies, starting with a simulation to validate the decision to omit the air boundary layer in Section 4.2. Section 4.3 shows the results of a validation study against a data set of PATER. The result of this study is also used to visualize the elastic waves within the cavity. The results of the simple transducer present in the model are briefly discussed in Section 4.5. The data set from PATER was initially generated to construct a cross-correlation map to measure spatial resolution. In Section 4.4, a similar cross-correlation map is made with simulation data and compared to the PATER map. Finally, in Section 4.6, the file sizes and computation times are shared for different 2D and 3D models.

4.1. Mesh Convergence Study

As discussed in Section 3.2.2, two values determining the mesh size should be tuned such that the solution is not dependent on the mesh size. First, the overall mesh size is found by varying the number of elements per wavelength. Second, a local mesh refinement study is performed to discretize the load distribution properly. The simulations were run for 5 µs, the excited area was located at the center of the imaging plane, the width of the Gaussian function was 50 µm, and the Amplitude was 1000 Pa.

The method to determine the mesh is to vary the number of elements per wavelength. This should result in a more general proof of the mesh size related to wavelength. A sequence of values was used for the value of epw, starting at 0.63 epw and increasing with a factor of 1.5 up to 3.56 epw. 1.5 epw is in the center of this range, and a good insight is thus generated in much smaller and larger elements compared to what is expected to be a good value. The prism size was 3 mm, a spot size of 50 µm was used and the simulation time was 5 µs.

Assuming that the signal measured with 3.56 epw is converged, we compared the other signals with this signal. The comparison is made by obtaining Pearson's product-moment correlation coefficient r, see Equation 4.3 [14]. r is a method to calculate the correlation between two signals where the amplitude difference is corrected. Convergence for the amplitude is measured using the root mean square (rms) value, and comparison is made by calculating the ratio of two rms values. The magnitude of the fluctuations of a signal can statistically be qualified by the rms value [15]. The rms ratio (RR) is thus a measure of the difference in magnitude.

Since COMSOL and the Nyquist sampling theorem suggest a value of epw between 1.5 and 2, it was also expected that the results would converge for a value of epw in this range. In Figure 4.1b, the r value for all the measured signals is plotted.

$$\overline{X} = \frac{1}{N}\sum_{n=1}^{N} X_i \tag{4.1}$$

$$\overline{Y} = \frac{1}{N}\sum_{i=1}^{N} Y_i \tag{4.2}$$

$$r = \frac{\sum_{i=1}^{N}((X_i - \overline{X})(Y_i - \overline{Y}))}{\sqrt{\sum_{i=1}^{N}(X_i - \overline{X})^2}\sqrt{\sum_{i=1}^{N}(Y_i - \overline{Y})^2}} \tag{4.3}$$

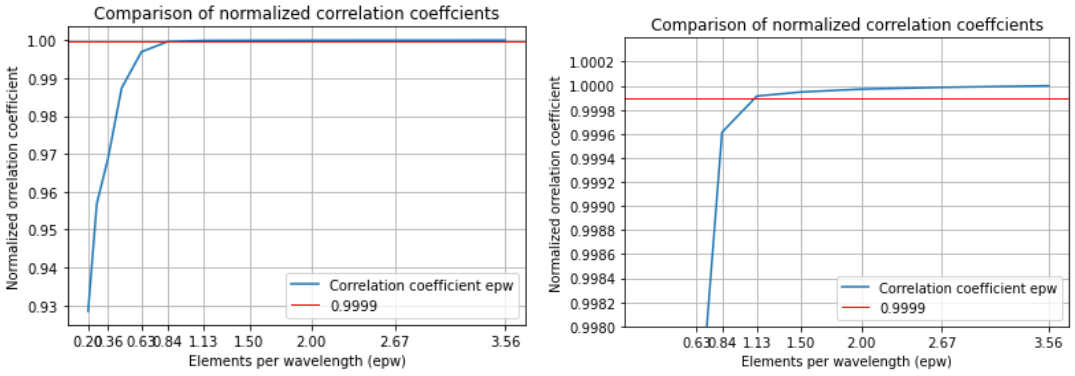

(a) **(b)**

Figure 4.1: a) Pearson's product-moment correlation coefficient r is shown on the y-axis. r is calculated between the signal for every value of epw and the last value of epw. Values for epw were, 0.2, 0.27, 0.36, 0.47. 0.63, 0.84, 1.13, 2.5, 2, 2.67, 3.56 **b)** The same graph as in a, but zoomed in for more accuracy.

Figure 4.1b shows that if we choose a value of 1.5 epw, the error will be lower than a factor $1e-4$. Interestingly, a value of 0.47 epw still gives a value of almost 0.99 for r. The calculated RR is plotted in Figure 4.2, convergence gets better after 2 epw. However, for 0.84 epw the error is already lower than 1 %.

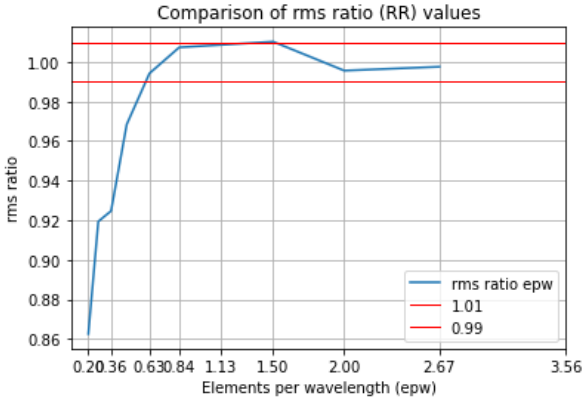

Figure 4.2: c is calculated between the signal for every value of epw and the last value of epw. Values for epw were, 0.2, 0.27, 0.36, 0.47. 0.63, 0.84, 1.13, 2.5, 2, 2.67, 3.56

Similarly, as for the general mesh refinement, the mesh at the location of the load is varied to find a value for which the signal converges. 1.5 epw is used for the general size. A sequence of values was used for ld, starting at 0.63 ld and increasing with a factor of 1.5 up to 3.56 ld. Again, we look at r and RR. The error in r is 0 for all values of ld higher than 0.63, and the error in RR is lower than $4e-4$; see Table 4.1.

For $ld = 0.5$, the mesh size of the load refinement is equal to the general mesh size; it is thus not needed to simulate smaller values of ld. A coarser mesh was chosen to examine the load refinement for smaller values of ld. The simulations were run with $epw = 0.5$. A sequence of values was used for ld, starting at 0.2 ld and increasing with a factor of 1.5 up to 0.84 ld. as can be seen in Table 4.2, the value of r converges relatively fast to an error lower than 1e-4 and RR quite fast to an error lower than 3e-3.

ld	0.63	0.84	1.13	1.5	2	2.67	3.56
RR	1.0004	1.0002	0.9998	0.9999	0.9999	1	1

Table 4.1: A rms ratio (RR) is calculated for the mesh refinement study of the load distribution

ld	0.2	0.27	0.32	0.47	0.63	0.84
r	0.9988	0.9999	0.9999	0.9999	0.9999	1
RR	2.0825	0.9997	0.9997	1.0162	1.0022	1

Table 4.2: Pearson's product-moment correlation coefficient r is calculated between the signal for every value of epw and the last value of epw. Similar the rms ratio (RR) is calculated.

For the simulations in the following sections, epw is set to 1.5 since the error for r is lower than $1e-4$ and the error for RR is lower than 0.01. ld is set to 0.5 since the error for r is 0 and the error for RR is lower than $4e-4$. The error limit is a bit arbitrary; if the simulation results are used for a specific case, there are two sources that help determine the required error limit. First, the sensitivity of the reconstruction algorithm to both r and RR must be known. Second, if an experimental dataset is used, there are many tolerances, and simulating with a very small error while having large tolerances in reality does not make any sense. Without having this information, we can only show the method to find the convergence for both r and RR and set a reasonable value for epw and ld for the following simulations.

4.2. Solid Air Interface

In reality, the prism is surrounded by air, and some part of the signal is refracted into the air domain. Modelling this domain will add a significant amount of elements since the speed of sound is an order of 10 lower compared to glass. Fortunately, the transmission coefficient is very low, $T_p = 6e-5$, as discussed in Section 2.5.1. It would be advantageous for the computational costs if the air domain is omitted. Therefore, a comparison is made between two simulations, one with an air domain and one without. Figure 4.3 shows the comsol model with air. The square and rectangular shapes surrounding the air domain are absorbing layers to mimic an infinite medium. The expectation is that the influence of the air domain on the measured signal is negligible. The simulations were run for 10 µs, the excited area was located at the center of the imaging plane, the width of the Gaussian function was 10 µm, and the Amplitude was 1000 Pa.

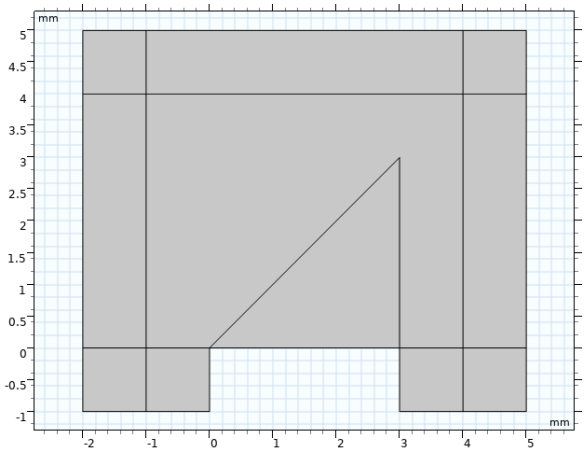

Figure 4.3: The figure shows the glass and air domain as modelled in COMSOL. The surrounding layer, built out of squares and rectangles, defines the absorbing layer to simulate an infinite medium.

As expected, the resulting two signals had a correlation coefficient of 0.999999. The ratio of the rms values of the two signals is 0.999.

4.3. Validation With Experimental data

Validation with experimental data is important to understand the differences between the COMSOL model and the real world. To validate the model, a comparison is made with a publicly available calibration dataset published in an Author manuscript of PATER [36]; the dataset can be found on a platform called figshare [53].

The main properties of this experiment are: a step size of 50 µm, a spot size of 10 µm, 40 x 40 pixels in

the center of the imaging plane, a measurement time of 164 µs, a sampling rate of 20 ns, and the sample consisted out of a drop of ink. The signal is recorded using a transducer with a center frequency of 10 MHz and 100 % one-way bandwidth.

The simulations were run for 25 µs, the excited area was located at the center of the imaging plane, the width of the Gaussian function was 50 µm, and the Amplitude was 1000 Pa.

Even though there are some major differences between the experimental setup and the COMSOL model, this is an opportunity to learn how the COMSOL model and experiment differ. This dataset is particularly suited because this kind of setup influences the boundary conditions at the image plane as little as possible. However, there are large differences between the two experiments. The most significant is the 2D and 3D difference. Another difference is that all nine edges were ground in a saw tooth pattern with a diamond saw. In addition, the input signal strength and shape of the PA signal are unknown. In this section, the comparison is done by plotting both signals and visually inspecting the differences. Due to the large differences, there is no meaning in calculating correlation coefficients or comparing amplitudes. The comparison mainly shows where the similarities are and checks whether this model is a realistic simulation of the imaging system.

To understand what happens inside the acoustic cavity, the waves are visualized using the signed square root of the second principal invariant of the stress tensor, as published in a COMSOL example [50]. In this way, the longitudinal waves (red) and shear waves (blue) are shown in a different colour; for a more detailed derivation of why this works, see Appendix E. For specific moments in time at the transducer surface, this visualization can help to understand the measurement signal; examples can be found in Appendix F.

Some peaks are expected to be measured at roughly the identical timestamps in the experiment and COMSOL. This is expected because there is some similarity in the shape of the boundaries. The frequency content should also be equal because our input signal does not exceed the bandwidth of the PATER transducer.

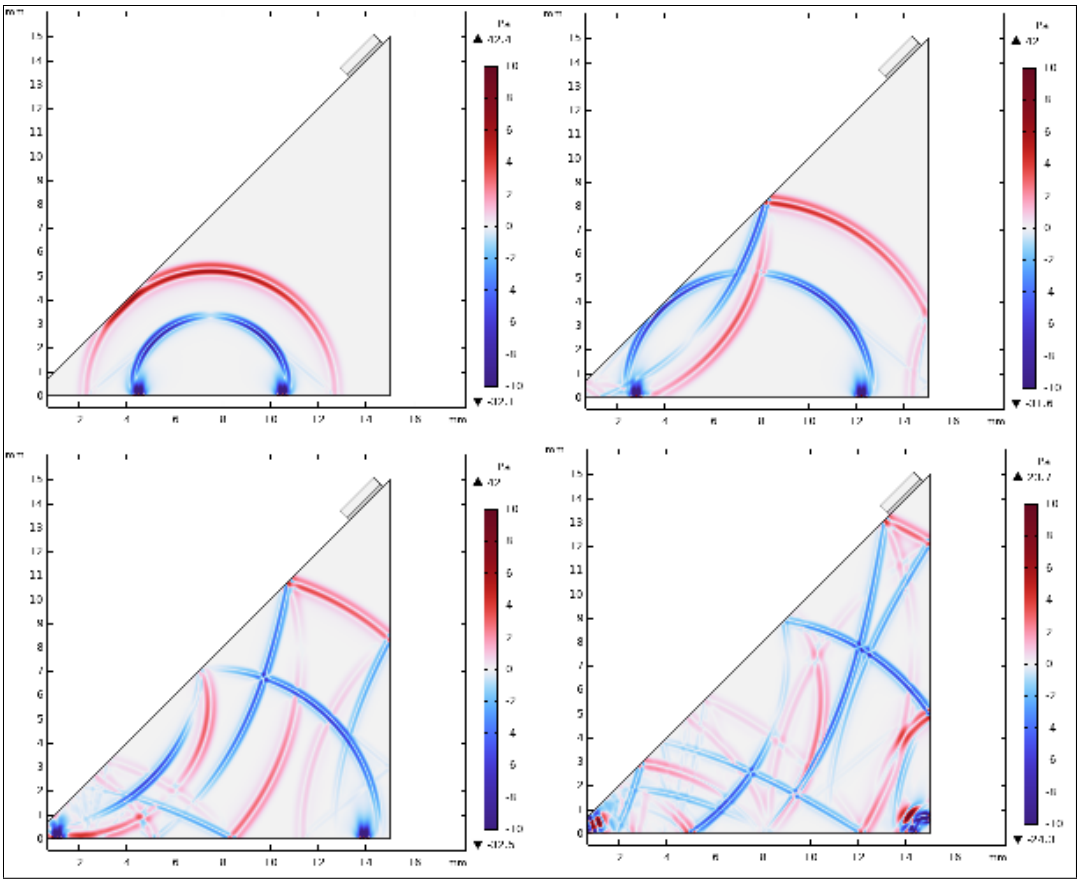

Figure 4.4: Wavefront propagation of the first two microseconds visualized, in red the longitudinal waves and in blue the shear waves.

The waves propagating in the cavity at 0.5, 1, 1.5, and 2 µs are shown in Figure 4.4. The three types of waves, longitudinal, transverse, and Rayleigh, can be seen just after the PA signal is generated. The mode conversion after reflections is also visible. Interestingly, surface waves are only generated at the PA signal start; they do propagate along certain edges and reflect as well. With certain conditions, they disappear; at least, they can not be seen any more in the plots. No new surface waves are generated.

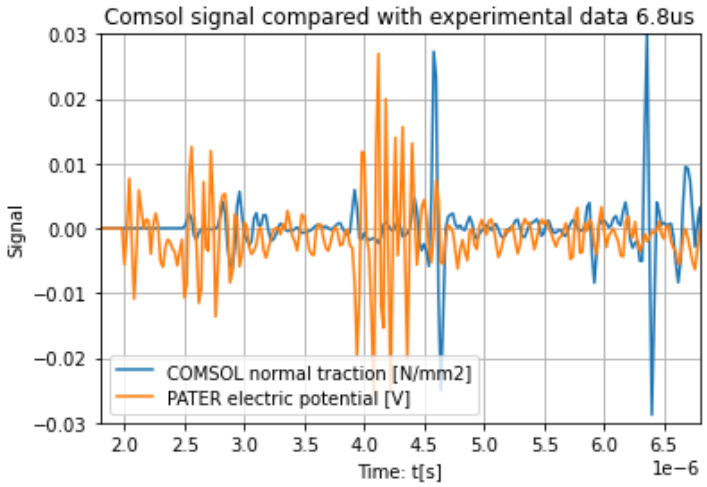

Figure 4.5: Comparison of an experimental impulse response and a COMSOL impulse response up to 6.8 µs. The COMSOL signal is scaled to the same amplitude by dividing it by 67.

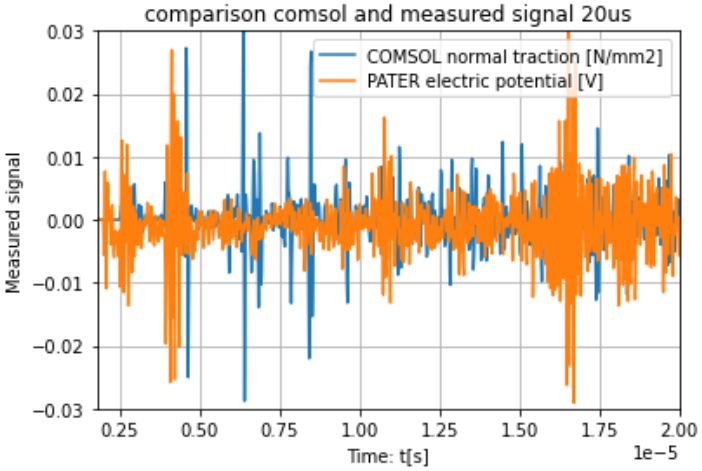

Figure 4.6: Comparison of a experimental impulse response and a COMSOL impulse response up to 20 µs. The COMSOL signal is scaled to the same amplitude by dividing it by 67.

The traction component normal to the transducer edge was used for comparison. Figure 4.5 and 4.6 show the Voltage signal from PATER and the normal traction of the COMSOL simulation. Before we could compare the two signals, the result from the COMSOL model is divided by a factor of 67 to obtain a similar amplitude for the first prominent peak. In Figure 4.5, the first peaks are at similar timestamps, and the wavelength looks similar at first sight too. The abundance of peaks in the PATER signal between 5 µs and 10 µs while there are high amplitude peaks in the COMSOL signal was not expected. This difference is clearly visible in Figure 4.6. On the contrary, around 16 µs, there is a prominent peak in the measurement of PATER, which is not visible in the COMSOL signal.

Finally, the frequency spectra of the three signals are compared to prove that we actually measure the same frequencies as we introduced and that this spectrum is also what the transducer in the PATER setup could measure. We expect similar bandwidths between the input signal, COMSOL, and PATER measurements.

If we look at Figure 4.7a, there is a lower frequency response up to 5 MHz and a lower response around 12 MHz compared to the COMSOL measurement, shown in Figure 4.7b. Since we do not have any frequency response data from the transducer manufacturer, we can not be certain why this response is visible in the results.

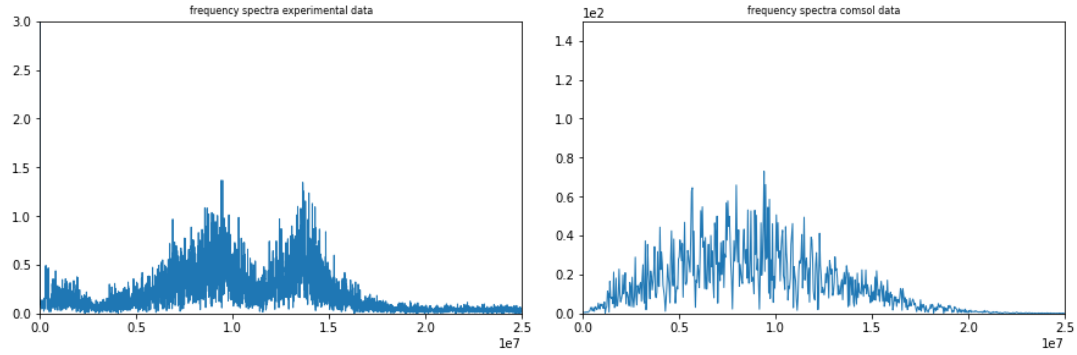

(a) (b)

Figure 4.7: a) The frequency spectrum of the PATER signal. **b)** The frequency spectrum of the COMSOL measurement.

4.4. Correlation Map

The working principle of the acoustic cavity is based on the characterization of each pixel and can be measured with a correlation map. A correlation map from the PATER manuscript [36] is shown in Figure 4.8a. The correlation map can be made by simulating all pixels and calculating the correlation with the center pixel. If our model works as intended, the correlation of signals should decrease with the distance from the center pixel.

The simulation is performed with a spot size of 50 µm for 40 pixels each 50 µm apart. The simulation time was set to 5 µs.

As shown in Figure 4.8b, this is true for the nearby pixels, but the correlation coefficient increases again further from the center. Although not a lot, this is not expected. The spatial resolution, taken as the FWHM of the center peak, is with 225 µm similar to PATER.

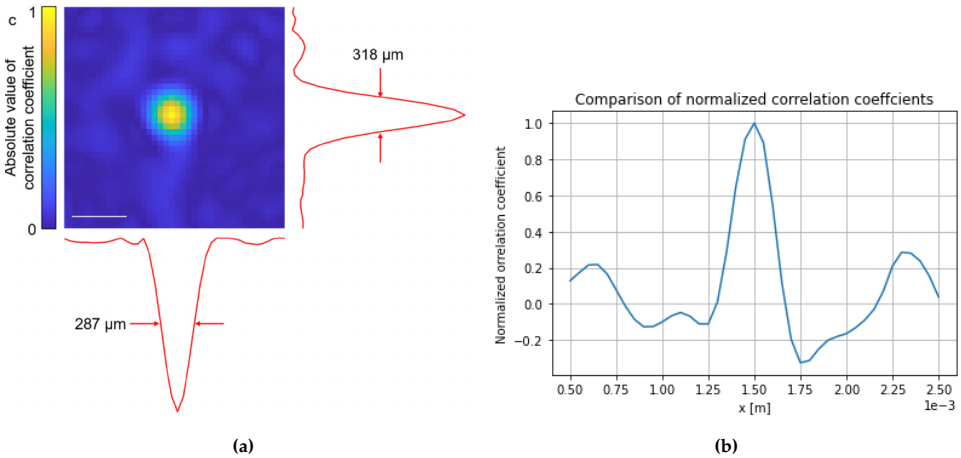

(a) (b)

Figure 4.8: a) A cross-correlation map of PATER, reproduced from [36]. **b)** A cross-correlation map of pixels with the center pixel, constructed with data from the COMSOL model.

4.5. The Transducer Model

A simple transducer is modelled to show the potential of COMSOL to simulate an actual piezo transducer for this process. Results of the validation simulation for the normal traction and terminal voltage of the transducer are compared to show this kind of model could aid the design of a transducer or generate more realistic simulation results, see Figure 4.9. Visually, the signals contain the same trends, and prominent peaks occur at equal time stamps. The correlation coefficient is 0.6.

In addition, two simple models are used to show the difference between a normal incidence, Figure 4.10a and Figure 4.11. And a 45° incidence, Figure 4.10b and Figure 4.12. For this measurement, the amplitude of the first peak of the terminal voltage was scaled to the first peak of the normal traction. The same scaling factor was used for the angled setup. It can be seen that the transducer model, compared to the normal traction, results in a similar measurement for the main longitudinal wavefront. However, the normal incidence result seems unstable after this wavefront, and in the angled situation, the transducer signal contains much smaller peaks. Although absorbing layers were used for most boundaries, some reflections were still occurring and caused the difference in measurement.

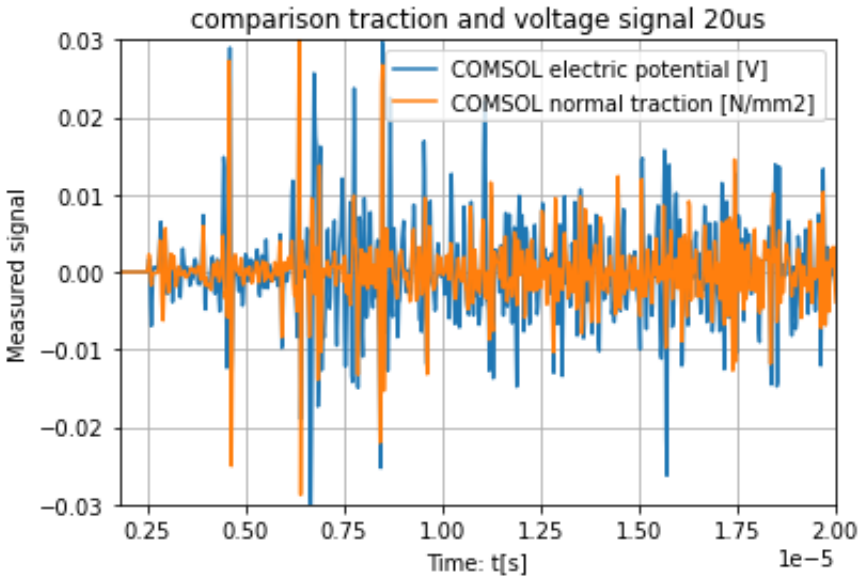

Figure 4.9: Comparison of the normal component of traction with the measured signal of the simple transducer. The correlation coefficient is 0.6.

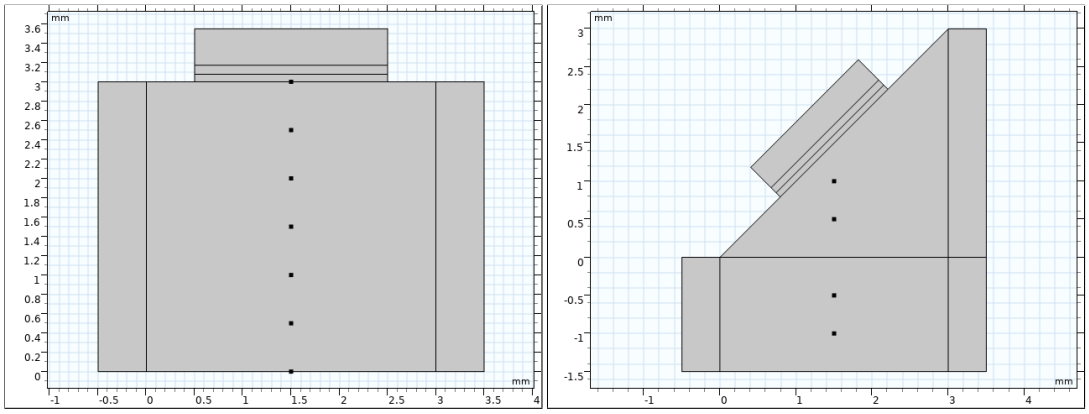

(a) **(b)**

Figure 4.10: a) Geometry of the simple horizontal setup with absorbing layers to decrease the number of reflections, b) Geometry of the simple angled setup with absorbing layers to decrease the number of reflections

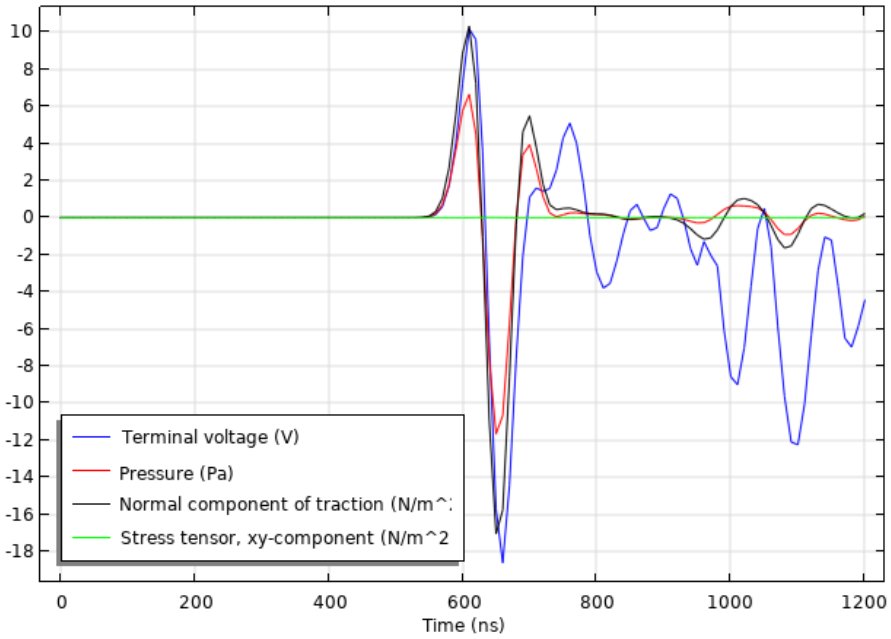

Figure 4.11: Results of the horizontal measurement, different values are plotted, the terminal voltage of the transducer, a line average of the pressure, a line average of the normal component of traction, and the shear component from the stress tensor.

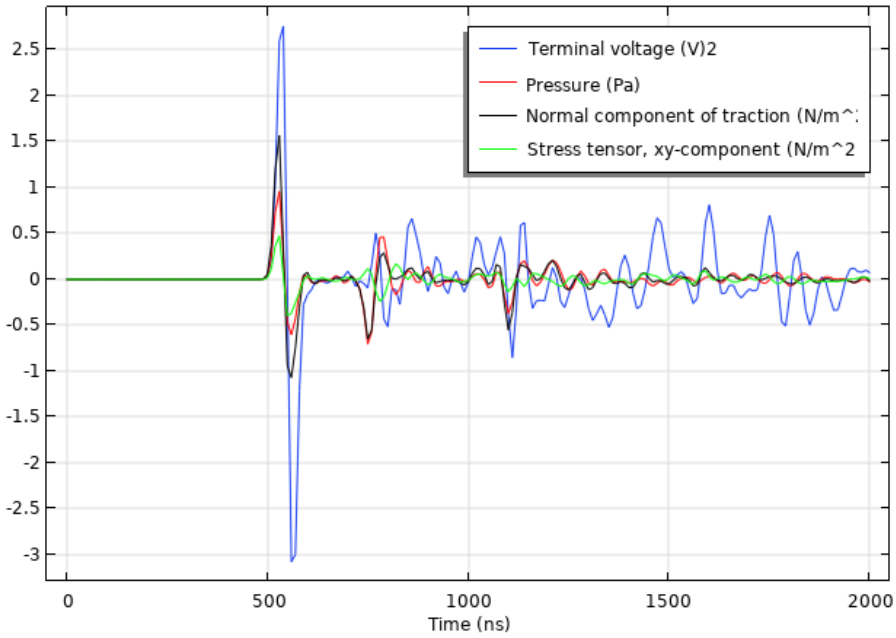

Figure 4.12: Results of the angled measurement, different values are plotted, the terminal voltage of the transducer, a line average of the pressure, a line average of the normal component of traction, and the shear component from the stress tensor.

4.6. Computation Time and File Sizes

The main issue with time-domain simulations is file size and computation time due to many elements and small solver time steps. This section uses the degree of freedom (DOF) to quantify the differences in computational costs between models. See figure 4.13a for the number DOF for different prisms. This section also shows the file sizes and computation times for the previous simulations. In addition, simulations are performed for 8, 16, 32, and 48 cores on the DelftBlue cluster to investigate the scaling in computation time. A 3 mm prism with a single PA signal was used, and a simulation time of 20 µs was used.

Table 4.3 shows the file sizes and computation times for various simulations. The platforms used are listed in Table 4.4. The main result from this table is that the 3mm prism can be simulated within an hour if the simulation time is lower than 15 µs. For the 2D 15mm case, the results differ quite a lot on the cluster and workstation but are within a few hours if the simulation time is lower than 20 µs. Some attempts have been made to simulate a 3D prism for validation; the results for a low epw value are also shown in the table. A similar effort has been made on DelftBlue for a value of 0.5 epw, but the simulation took 24 h and was only at 86 %. Unfortunately, masters students can not run simulations longer than 24 h with a maximum of 48 cores.

size	2D/3D	mesh size	duration	file size	computation time	platform	cores
3mm	2D	1.5 epw	5 µs	0.5 GB	20 min	laptop	6
3mm	2D	1.5 epw	20 µs		330 min	cluster	8
15mm	2D	1.5 epw	10 µs	25 GB	90 min	workstation	4
15mm	2D	1.5 epw	20 µs	1.3 GB or 40 GB	420 min	cluster	16
15mm	2D	1.5 epw	20 µs	1.3 GB or 40 GB	240 min	cluster	32
15mm	3D	0.15 epw	10 µs	0.5 GB	50 min	workstation	4
15mm	3D	0.25 epw	10 µs	0.5 GB	450 min	workstation	4
15mm	3D	0.5 epw	10 µs	–	– (>24 h)	cluster	48

Table 4.3: Performance with regards to the computational costs for different simulations performed throughout this project.

type	brand	CPU	clockspeed	cores	RAM
workstation	Dell precision T3600	Intel Xeon E5-1620	3.6GHz	4	64GB
laptop	HP Zbook studio G5	Intel core i7-8750H	2.2GHz	6	16GB
cluster	DelftBlue	max. 2x Intel Xeon E5-6248R	3.0GHz	max. 48	max. 192GB

Table 4.4: Different platforms are shown that were used for the computations. The workstation is around 10 years old and the laptop is 5 years old.

In Figure 4.13b, the scaling of the computation time is shown with respect to a simulation done with eight cores. For eight cores, the simulation time was 5.5 h. The graph shows that the scaling with 48 cores is still good. Due to the maximum number of cores that master students are allowed to use, further scaling could not be investigated.

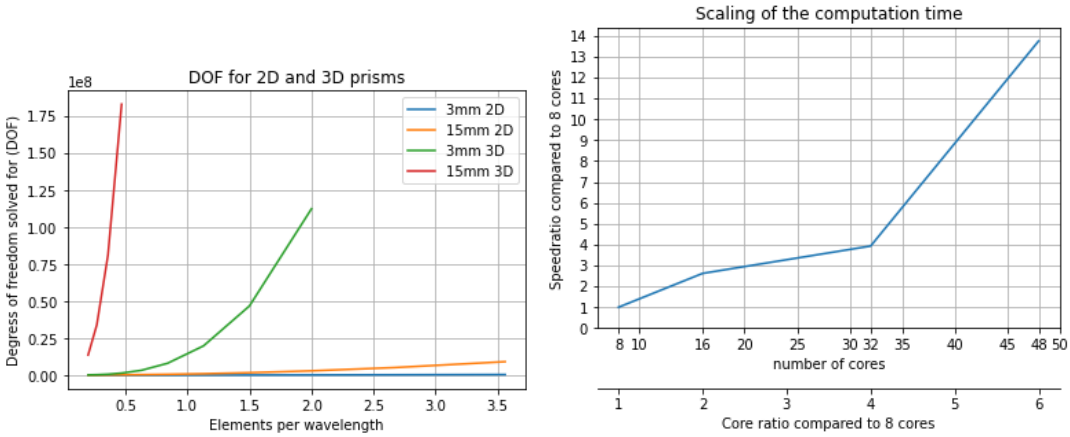

(a) (b)

Figure 4.13: a) The degrees of freedom are shown for different prism in 2D and 3D, using 4th order elements against different values for epw. **b)** The scaling of the computation time is shown for a 3mm prism simulated for 20 µs

4.7. Summary

Finite element methods in a time-dependent study containing high-frequency signals are time-consuming because the small mesh size causes a large DOF number and small solver time steps. COMSOL advice and the Nyquist sample theorem give approximations for the element size. To find an as large as possible value for the elements, the first studies were mesh convergence studies. In this report, the element size is not used directly. The variable, elements per wavelength (epw), is used to obtain a more general result; in addition, a variable ld represents the number of samples per FWHM of the distributed load (If Gaussian). No mesh convergence study was performed with regard to the thin layers of the transducer. The signals are compared with two values. First, to compare the signals, independent of amplitude, Pearson's product-moment correlation coefficient r was calculated between a (assumed) converged signal. Second, the root mean square (rms) ratio between this converged signal was calculated. The results in Section 4.1 showed a fast convergence. For the simulations in the following sections, epw is set to 1.5 since the error for r is lower than $1e-4$ and the error for RR is lower than 0.01. ld is set to 0.5 since the error for r is 0 and the error for RR is lower than $4e-4$.

When the model was constructed, it was assumed that the air domain surrounding the prism could be omitted because the reflection coefficient was 0.9999. A vibroacoustic model was built to verify this assumption. In Section 4.2, the results are presented. As expected, the resulting two signals had a correlation coefficient of 0.999999. The ratio of the rms values of the two signals is 0.999.

For this project, it was impossible to set up validation experiments. Fortunately, a dataset from a PATER study has been published. This dataset is used to validate the model. Due to the significant differences between the numerical model and the PATER experiment, the correlation of the results was very low. Three other methods have been used instead: a visual inspection of the wave propagation and behaviour, a visual comparison of prominent peaks in both simulations, and a comparison of the cross-correlation map with respect to a center pixel. In Section 4.3, plots show three wave types, mode conversions and different wave speeds. A comparison of the normal traction and the Voltage signal showed a similarity of the first wavefronts; in addition, the frequency spectra showed that our input signal indeed represents the measured signal from PATER. The comparison of the cross-correlation map in Section 4.4 showed that the COMSOL model performed almost equally compared to the experimental data. Not expected were the extra side lobes visible in the plot, indicating an increased correlation between pixels.

A simple transducer is modelled to show the potential of COMSOL to simulate an actual piezo transducer for this process. Results of the validation simulation for the normal traction and terminal voltage of the transducer are compared to show this kind of model could aid the design of a transducer or generate more realistic simulation results, see Figure 4.9. Visually, the signals contain the same trends, and prominent peaks occur at equal time stamps. Two simple simulations show that the measurement of a single wavefront is similar in shape but differs in amplitude. Although absorbing layers were used

for most boundaries, some reflections still occurred and caused differences in measurement.

The performance data of the previous simulations were collected in combination with two other studies, namely a DOF number generation study and a cluster scaling study, to show how the different model settings perform. In Section 4.6, the results are displayed. The main result is that a 2D 3mm and 15mm prism can be simulated within a couple of hours. 3D simulations are much more costly; 15 mm 3D simulations are not possible for a student with limited resources on the DelftBlue cluster. Expected but not tested, is that 3mm 3D simulations are possible on the cluster as a student. It should be noted that results differ greatly depending on the platform used; for instance, the older workstation, which has four cores, seems to be much faster than the same simulation on a cluster using 32 cores. In Figure 4.13b, the scaling of the computation time is shown with respect to a simulation done with eight cores. For eight cores, the simulation time was 5.5 h. The graph shows that the scaling with 48 cores is still good. Due to the maximum number of cores that master students can use, further scaling could not be investigated.

5
Discussion and Conclusion

A model has been built, tuned and tested; the main properties are the DG-FEM method, a highly tunable, but representative, load distribution and a basic geometry without a surrounding air domain. The interface used in COMSOL can simulate elastic waves and can be coupled to other interfaces such as pressure waves, electrostatics, and heat transfer. The load distribution can be modified such that a single PA source is simulated or multiple. Both the calibration and imaging modes can thus be tested.

As expected, the mesh converged for values of 1.5 epw and 0.5 ld, but the mesh convergence study results showed an earlier convergence than expected. An explanation can be found in the frequency used to approximate the mesh size. In Figure 3.2b, it can be seen that the peak of the spectrum is at 5 MHz, while we used 20 MHz for approximating the mesh size. The power of the higher frequencies is lower, and a large part of the measurement is probably determined by lower frequencies, which explains the convergence for larger mesh sizes.

Since general variables are used for qualifying the convergence, it is easy to calculate the mesh sizes for another studies. We advice to use low values for epw and ld to test a model, since the results are approaching the converged value quite fast. Low values allows for faster computation times and thus the ability to check a model before it runs multiple hours.

The measurement signal of COMSOL was divided by a factor of 67 to obtain similar amplitudes as the PATER measurement. Four mechanisms can explain this difference. First, we have the difference in spreading, proportional to $\sqrt{r}$, and equal to 4 if a distance of15 mm is travelled. Second, the signal of PATER is amplified by 48 DB, equal to a factor of 250. Third, the signal from COMSOL is in Volts, while the signal of PATER is in N/m^2. Since we don't know the sensitivity of the transducer used for PATER, the sensitivity of a similar type of transducer is used (reference needed). This transducer has a sensitivity of $0.85\,\mathrm{mV\,kPa^{-1}}$. Fourth, the input signal strength is unknown. All those effects make it hard to compare the amplitude. Fortunately, the amplitude difference between PATER and the COMSOL model is not of much importance when testing the performance of the model. If more details about the experiment are known, a better estimation of the expected amplitude can be made.

The visualization of the elastic waves showed all expected wave types and mode conversion behaviour. Although the first peaks of the signals were at similar time stamps and the frequency content was equal, comparing the 2D and 3D cases did not result in a good correlation. The conditions for when a strong signal is measured are related to the incident angle, which is probably very different for the 2D and 3D cases. In addition, the directionality of the transducers might be very different. However, the visualization, similar first peaks, and same frequency spectra showed that the model could simulate a realistic case. Since COMSOL is not limited to the wave types referred to in this report, acoustic cavity shapes where other wave types are more dominant can also be researched with this model. For instance, members of the research group are investigating the use of microscopic glasses as acoustic cavity. In the microscopic glass, Lamb waves are dominant due to the thickness of the glass relative to the wavelength. This model can easily be changed to study such a case.

Specifically for the PATER case, the cross-correlation map was almost equal and, thus, showed the same ability to characterize each pixel. Not expected were the side lobes in the cross-correlation map. The authors of PATER stated that more reflections lead to a higher resolution. Since our model has fewer planes, no ground edges and a shorter simulation time, there are also much fewer reflections. This might be a reason for the side lobes occurring in the COMSOL result. Still, the resolution should be almost equal and the model should be able to reproduce images with the same resolution.

A brief attempt was made to model a piezoelectric model, but the results of the transducer were not closer to the PATER data as was hoped for compared to the normal component of traction. The main

reason for the transducer model not performing better than the traction can be found in the difference between the PATER transducer and this model and in the not-so-well-designed model. The PATER uses a piezo element in a housing brought in contact via a high-impedance gel with the prism. The COMSOL model is a piezo patch affixed to the surface of the prism. This means that PATER can probably only measure longitudinal waves, whereas the model we used can be directly influenced by transverse waves and Rayleigh waves. In addition, the material and dimensions are probably not equal, and thus, the two transducers have a different center frequency, bandwidth, directionality, and sensitivity. If a similar transducer architecture will be used, a COMSOL model, but better designed, can aid the design or validate experimental results.

Besides the validity of the model, the computational costs are essential for a good model. If those costs are too high due to very large file sizes and long computation times, using the model is not easy. At the start, decisions were made to limit the computational costs, and studies were done to limit the number of elements and to keep the size as large as possible. The main result is that a 2D 3mm and 15mm prism can be simulated within a couple of hours. 3D simulations are much more costly; 15 mm 3D simulations are not possible for a student with limited resources on the DelftBlue cluster. Expected but not tested is, based on the DOF, that performing 3mm 3D simulations is possible on the DelftBlue cluster as a student.

The scaling of the model is, with 48 cores, good. Due to the maximum number of cores that master students can use, further scaling could not be investigated. Based on the graph, more cores could still be beneficial and should be tried, especially for 3D simulations. If enough resources are available this gives the ability to simulate small 3D objects such as an 3mm prism. It should be noted that the platform used for simulation is important. COMSOL is not good at parallelizing, as can be seen in the computation times. The workstation with four cores is much faster than the cluster simulation with 32 cores.

We thus showed how to built, tune and test a model in COMSOL that simulates a PA signal source or sources and the measurement of the initial wavefront and its reflections in a acoustic cavity. Although validating with experimental data was difficult so far, using the model to aid the design of a new high performance endoscope is definitely possible.

6
Recommendations and Future Work

If this model is used for experimental validation, the experimental setup could be adjusted such that reflections from planes that do not exist in the 2D model take a very long time to reach the transducer, or not at all by changing the boundary conditions of those planes, e.g. adding a impedance matching layer with a high absorption coefficient. For instance, an experimental set up to validate the COMSOL model, would be to use a long prism where the transducer is located vertically above the PA source.

The corners of our prism are sharp and not realistic. Peak stresses might occur at the corners due to the way they are modelled. The reason when the geometry was built was that adding small features like chamfers or fillets would decrease the mesh in size locally. No effort has been made to find whether the the measurement signal is sensitive to changes of these corners. A small study can be conducted to investigate this.

The design of a good transducer model was not in the scope of this project. There is, however, a lot of knowledge available for transducers in the field of non destructive testing. It would be interesting to investigate the options of modelling a better transducer with the knowledge from this field of engineering.

Small prisms of 3mm exist and if a small transducer is designed that is affixed to the prism, the model can be used to aid this design and validate the experimental results.

References

[1] G. Diebold, T. Sun, and M. Khan, "Photoacoustic monopole radiation in one, two, and three dimensions," *Physical review letters*, vol. 67, no. 24, p. 3384, 1991.

[2] K. F. Graff, *Wave motion in elastic solids*. New York: Dover, 1991, 649 pp., Originally published: Oxford: Clarendon Press, 1975. - Includes bibliographical references and indexes, ISBN: 0486667456.

[3] G. Diebold and T. Sun, "Properties of photoacoustic waves in one, two, and three dimensions," *Acta Acustica united with Acustica*, vol. 80, no. 4, pp. 339–351, 1994.

[4] M. Khan and G. Diebold, "The photoacoustic effect generated by an isotropic solid sphere," *Ultrasonics*, vol. 33, no. 4, pp. 265–269, 1995.

[5] L. E. Kinsler, Ed., *Fundamentals of acoustics*, 4th ed. New York: Wiley, 2000, 1548 pp., Includes bibliographical references and index. - Print version record, ISBN: 1523117885.

[6] J. Bioucas-Dias and M. Figueiredo, "A new twist: Two-step iterative shrinkage/thresholding algorithms for image restoration," *IEEE Transactions on Image Processing*, vol. 16, no. 12, pp. 2992–3004, Dec. 2007, ISSN: 1941-0042. DOI: 10.1109/tip.2007.909319.

[7] A. Beck and M. Teboulle, "A fast iterative shrinkage-thresholding algorithm for linear inverse problems," *SIAM Journal on Imaging Sciences*, vol. 2, no. 1, pp. 183–202, Jan. 2009, ISSN: 1936-4954. DOI: 10.1137/080716542.

[8] R. A. Webster, "Passive materials for high frequency piezocomposite ultrasonic transducers," Ph.D. dissertation, University of Birmingham, 2010.

[9] P. Beard, "Biomedical photoacoustic imaging," *Interface Focus*, vol. 1, no. 4, pp. 602–631, May 2011, ISSN: 2042-8901. DOI: 10.1098/rsfs.2011.0028.

[10] J. D. N. Cheeke, *Fundamentals and applications of ultrasonic waves*, 2nd ed (Online-Ausg.) Boca Raton: CRC Press, 2012, 1473 pp., Includes bibliographical references. - Description based on print version record, ISBN: 9781280687693.

[11] L. V. Wang, *Biomedical Optics, Principles and Imaging*, H.-i. Wu, Ed. Chicester: Wiley, 2012, 378 pp., Description based upon print version of record, ISBN: 9780471743040.

[12] L. V. Wang and S. Hu, "Photoacoustic tomography: In vivo imaging from organelles to organs," *Science*, vol. 335, no. 6075, pp. 1458–1462, Mar. 2012. DOI: 10.1126/science.1216210.

[13] L. Xi, S. R. Grobmyer, and L. Wu, "Evaluation of breast tumor margins in vivo with intraoperative photoacoustic imaging," 2012.

[14] M.-T. Puth, M. Neuhäuser, and G. D. Ruxton, "Effective use of pearson's product–moment correlation coefficient," *Animal Behaviour*, vol. 93, pp. 183–189, Jul. 2014, ISSN: 0003-3472. DOI: 10.1016/j.anbehav.2014.05.003.

[15] R. S. Figliola and D. E. Beasley, *Theory and design for mechanical measurements*, 6. ed. Hoboken, NJ: Wiley, 2015, 614 pp., Previous edition: 2011. - Formerly CIP. - Includes bibliographical references and index, ISBN: 9781118881279.

[16] L. V. Wang and J. Yao, "A practical guide to photoacoustic tomography in the life sciences," *Nature Methods*, vol. 13, no. 8, pp. 627–638, Jun. 2016. DOI: 10.1038/nmeth.3925.

[17] S. C. and A. K. Thittai, "Simulation of photoacoustic tomography (pat) system in comsol and comparison of two popular reconstruction techniques," in *SPIE Proceedings*, A. Krol and B. Gimi, Eds., SPIE, Mar. 2017. DOI: 10.1117/12.2254450.

[18] A. Seki, K. Iwai, T. Katagiri, and Y. Matsuura, "Sensitivity improvement of optical fiber acoustic probe for all-optical photoacoustic imaging system," *Applied Physics Express*, vol. 10, no. 7, p. 072 503, Jun. 2017. DOI: 10.7567/apex.10.072503.

[19] R. Ansari, E. Z. Zhang, A. E. Desjardins, and P. C. Beard, "All-optical forward-viewing photoacoustic probe for high-resolution 3d endoscopy," *Light: Science and Applications*, vol. 7, no. 1, Oct. 2018, ISSN: 2047-7538. DOI: 10.1038/s41377-018-0070-5.

[20] Y.-H. Liu, Y. Xu, L.-D. Liao, K. C. Chan, and N. V. Thakor, "A handheld real-time photoacoustic imaging system for animal neurological disease models: From simulation to realization," *Sensors*, vol. 18, no. 11, p. 4081, Nov. 2018, ISSN: 1424-8220. DOI: 10.3390/s18114081.

[21] S. Jeon, J. Kim, D. Lee, J. W. Baik, and C. Kim, "Review on practical photoacoustic microscopy," *Photoacoustics*, vol. 15, p. 100 141, Sep. 2019, ISSN: 2213-5979. DOI: doi:10.1016/j.pacs.2019.100141.

[22] G. Li, Z. Guo, and S.-L. Chen, "Miniature probe for forward-view wide-field optical-resolution photoacoustic endoscopy," *IEEE Sensors Journal*, vol. 19, no. 3, pp. 909–916, Feb. 2019, ISSN: 2379-9153. DOI: 10.1109/jsen.2018.2878801.

[23] D.-Y. Yang, Y. Zhu, J.-Q. Kong, *et al.*, "Light in and sound out: Review of photoacoustic imaging in cardiovascular medicine," *IEEE Access*, vol. 7, pp. 38 890–38 901, 2019. DOI: 10.1109/ACCESS.2019.2902543.

[24] T. Zhao, A. E. Desjardins, S. Ourselin, T. Vercauteren, and W. Xia, "Minimally invasive photoacoustic imaging: Current status and future perspectives," *Photoacoustics*, vol. 16, p. 100 146, Dec. 2019. DOI: 10.1016/j.pacs.2019.100146.

[25] R. Ansari, E. Z. Zhang, A. E. Desjardins, and P. C. Beard, "Miniature all-optical flexible forward-viewing photoacoustic endoscopy probe for surgical guidance," *Optics Letters*, vol. 45, no. 22, p. 6238, Nov. 2020, ISSN: 1539-4794. DOI: 10.1364/ol.400295.

[26] S. A. S. El-Busaidy, B. Baumann, M. Wolff, and L. Duggen, "Modelling of open photoacoustic resonators," *Photoacoustics*, vol. 18, p. 100 161, Jun. 2020, ISSN: 2213-5979. DOI: 10.1016/j.pacs.2020.100161.

[27] H. Guo, Y. Li, W. Qi, and L. Xi, "Photoacoustic endoscopy: A progress review," *Journal of Biophotonics*, vol. 13, no. 12, Jul. 2020, ISSN: 1864-0648. DOI: DOI:10.1002/jbio.202000217.

[28] M. Kaur, P. M. Lane, and C. Menon, "Endoscopic optical imaging technologies and devices for medical purposes: State of the art," *Applied Sciences*, vol. 10, no. 19, p. 6865, Jul. 2020, ISSN: 2076-3417. DOI: 10.3390/app10196865.

[29] Y. Li, L. Li, L. Zhu, *et al.*, "Snapshot photoacoustic topography through an ergodic relay for high-throughput imaging of optical absorption," *Nature Photonics*, vol. 14, no. 3, pp. 164–170, Jan. 2020. DOI: 10.1038/s41566-019-0576-2.

[30] S. Mezil, A. M. Caravaca-Aguirre, E. Z. Zhang, *et al.*, "Single-shot hybrid photoacoustic-fluorescent microendoscopy through a multimode fiber with wavefront shaping," *Biomedical Optics Express*, vol. 11, no. 10, p. 5717, Sep. 2020. DOI: 10.1364/boe.400686.

[31] V. T. Rathod, "A review of acoustic impedance matching techniques for piezoelectric sensors and transducers," *Sensors*, vol. 20, no. 14, p. 4051, Jul. 2020, ISSN: 1424-8220. DOI: 10.3390/s20144051.

[32] W. Zhang, H. Ma, Z. Cheng, Z. Wang, K. Xiong, and S. Yang, "High-speed dual-view photoacoustic imaging pen," *Optics Letters*, vol. 45, no. 7, p. 1599, Mar. 2020. DOI: 10.1364/ol.388863.

[33] J. Zhou and J. V. Jokerst, "Photoacoustic imaging with fiber optic technology: A review," *Photoacoustics*, vol. 20, p. 100 211, Dec. 2020. DOI: 10.1016/j.pacs.2020.100211.

[34] S.-W. Cho, S. M. Park, B. Park, *et al.*, "High-speed photoacoustic microscopy: A review dedicated on light sources," *Photoacoustics*, vol. 24, p. 100 291, Dec. 2021, ISSN: 2213-5979. DOI: 10.1016/j.pacs.2021.100291.

[35] M. Kaur, P. M. Lane, and C. Menon, "Scanning and actuation techniques for cantilever-based fiber optic endoscopic scanners a review," *Sensors*, vol. 21, no. 1, p. 251, Jan. 2021, ISSN: 1424-8220. DOI: 10.3390/s21010251.

[36] L. Li, Y. Li, Y. Zhang, and L. V. Wang, "Snapshot photoacoustic topography through an ergodic relay of optical absorption in vivo," *Nature Protocols*, vol. 16, no. 5, pp. 2381–2394, Apr. 2021, ISSN: 1750-2799. DOI: 10.1038/s41596-020-00487-w.

[37] Y. Li, G. Lu, Q. Zhou, and Z. Chen, "Advances in endoscopic photoacoustic imaging," *Photonics*, vol. 8, no. 7, p. 281, Jun. 2021. DOI: 10.3390/photonics8070281.

[38] D. Biswas, S. Roy, and S. Vasudevan, "Biomedical application of photoacoustics: A plethora of opportunities," *Micromachines*, vol. 13, no. 11, p. 1900, Nov. 2022, ISSN: 2072-666X. DOI: 10.3390/mi13111900.

[39] Y. Zhang, H. Wei, and H. Fang, "Photoacoustic waves of a fluidic elliptic cylinder: Analytic solution and finite element method study," *Frontiers in Physics*, vol. 10, Sep. 2022, ISSN: 2296-424X. DOI: 10.3389/fphy.2022.960165.

[40] T. Zhao, T. T. Pham, C. Baker, *et al.*, "Ultrathin, high-speed, all-optical photoacoustic endomicroscopy probe for guiding minimally invasive surgery," *Biomedical Optics Express*, vol. 13, no. 8, p. 4414, Jul. 2022. DOI: 10.1364/boe.463057.

[41] T. Zhao, M. Zhang, S. Ourselin, and W. Xia, "Wavefront shaping-assisted forward-viewing photoacoustic endomicroscopy based on a transparent ultrasound sensor," *Applied Sciences*, vol. 12, no. 24, p. 12 619, Dec. 2022. DOI: 10.3390/app122412619.

[42] M. T. GadAllah, A. E.-N. A. Mohamed, A. A. Hefnawy, H. E. Zidan, G. M. El-Banby, and S. M. Badawy, "A mathematical model for simulating photoacoustic signal generation and propagation in biological tissues," *Optical and Quantum Electronics*, vol. 56, no. 1, Nov. 2023, ISSN: 1572-817X. DOI: 10.1007/s11082-023-05481-6.

[43] H. He, L. Englert, and V. Ntziachristos, "Optoacoustic endoscopy of the gastrointestinal tract," *ACS Photonics*, vol. 10, no. 3, pp. 559–570, Feb. 2023, ISSN: 2330-4022. DOI: 10.1021/acsphotonics.2c01264.

[44] D. Ke, L. Wang, E. Wang, H. Xin, S. Yang, and K. Xiong, "Miniature fiber scanning probe for flexible forward-view photoacoustic endoscopy," *Applied Physics Letters*, vol. 122, no. 12, p. 123 703, Mar. 2023, ISSN: 1077-3118. DOI: 10.1063/5.0142792.

[45] S. N. Thakur, D. Pandey, and S. N. Rai, "Applications of photoacoustic spectroscopy and imaging in gastroenterology," in *Photoacoustic and Photothermal Spectroscopy*, Elsevier, 2023, pp. 571–586. DOI: 10.1016/b978-0-323-91732-2.00001-x.

[46] B. Yan, B. Song, G. Mu, Y. Fan, and Y. Zhao, "Compressed single-shot 3d photoacoustic imaging with a single-element transducer," *Photoacoustics*, vol. 34, p. 100 570, Dec. 2023, ISSN: 2213-5979. DOI: 10.1016/j.pacs.2023.100570.

[47] Y. Zhang, P. Hu, L. Li, *et al.*, "Ultrafast longitudinal imaging of haemodynamics via single-shot volumetric photoacoustic tomography with a single-element detector," *Nature Biomedical Engineering*, Nov. 2023, ISSN: 2157-846X. DOI: 10.1038/s41551-023-01149-4.

[48] Y. Zhao and L. V. Wang, "Single-shot photoacoustic imaging with single-element transducer through a spatiotemporal encoder," *Journal of Biomedical Optics*, vol. 28, no. 04, Apr. 2023. DOI: 10.1117/1.jbo.28.4.046004.

[49] COMSOL, *Comsol*, COMSOL, https://www.comsol.com/.

[50] COMSOL, *Comsol example: Ground motion seismic event*, COMSOL. [Online]. Available: https://doc.comsol.com/6.1/doc/com.comsol.help.models.aco.ground_motion_seismic_event/ground_motion_seismic_event.html#545481.

[51] COMSOL, *Meshing and solving elastic waves, time explicit models.* COMSOL. [Online]. Available: https://doc.comsol.com/6.2/docserver/#!/com.comsol.help.aco/aco_ug_elastic_waves.06.51.html.

[52] k-wave, *K-wave*, k-wave, http://www.k-wave.org/documentation.php.

[53] L. Li, Y. Li, Y. Zhang, and L. V. Wang, "Dataset figure 2, from: Snapshot photoacoustic topography through an ergodic relay of optical absorption in vivo," [Online]. Available: https://figshare.com/articles/dataset/Data_for_Fig_2/12950798.

A

State of the Art PAE

For the calculation of the fast C scan rate the following parts are assumed ideal: the speed of the scanning mechanism, the data acquisition system, computational power, and refresh rates of a DMD or SLM. Two new variables are introduced f_{Cfast} which represents the frame rate of the system closest to real time or real time, and PRR_{Cfast} which represents the PRR needed for f_{Cfast}. See below for the method to calculate these variables.

c	$\mathrm{m\,s^{-1}}$	speed of sound
d	m	depth of view
PRR_{Cmax}	pulses per second	maximum pulse repetition rate
f_{Cmax}	frames per second	maximum frame rate
$N_{samples}$	[-]	number of samples on surface
pa	[-]	pulse averaging
f_{Cfast}	frames per second	fast frame rate
PRR_{Cfast}	frames per second	fast pulse repetition rate

$$PRR_{Cmax} = \frac{c}{d}$$

$$f_{Cmax} = \frac{PRR_{Cmax}}{N_{samples} * pa}$$

$$\begin{aligned} if \quad & (f_{Cmax} < 20): \\ & f_{Cfast} = f_{Cmax} \\ & PRR_{Cfast} = PRR_{Cmax} \\ else: & \\ & f_{Cfast} = 20 \\ & PRR_{Cfast} = f_{Cmax} * N_{samples} \end{aligned}$$

	$N_{samples}$[-]	d[mm]	pa[-]	PRR_{Cfast} [kHz]	f_{Cfast} [Hz]
SMF + grin lens [22]	688900	6.38	16	241	0.02
SMF + hollow fibre [18]	127	1	128	325	20
SMF + flexible PACT [25]	3000	8	1	60	20
SMF + rigid PACT [19]	45000	7	1	220	5
Hollow tube [32]	5152	1	1	103	20
MMF 1 [41]	10000	1	64	1540	2.4
MMF 2 [40]	7854	1	1	157	20
MMF 3 [30]	1800	1	1	36	20
fibre scanner [44]	100000	1	1	1540	15.4
MEMS scanner [13]	2500	2.3	1	50	20

Table A.1: Showing whether it is possible to have real time imaging capabilities, and what PRR is needed in that case.

B
Acoustic Waves

B.1. Wave Types

Acoustic waves can propagate in fluids(including gases) and solids. Within fluids, only pressure waves, or longitudinal waves, are present. While in solids other wave types occur as well. The different types are mainly characterized by the particle motion relative to the wave direction. The three types of waves expected in the acoustic cavity are longitudinal waves, transverse waves, and Rayleigh waves. The particle motion relative to the wave direction is shown in Figure B.1. Longitudinal waves and transverse waves occur in the entire solid domain, while Rayleigh waves only travel approximately a wavelength distance from the surface [10]. For longitudinal waves, the wave direction is parallel to the particle movement; for transverse waves, the particle motion is perpendicular to the wave motion; and the particle movement for Rayleigh waves has an oval shape.

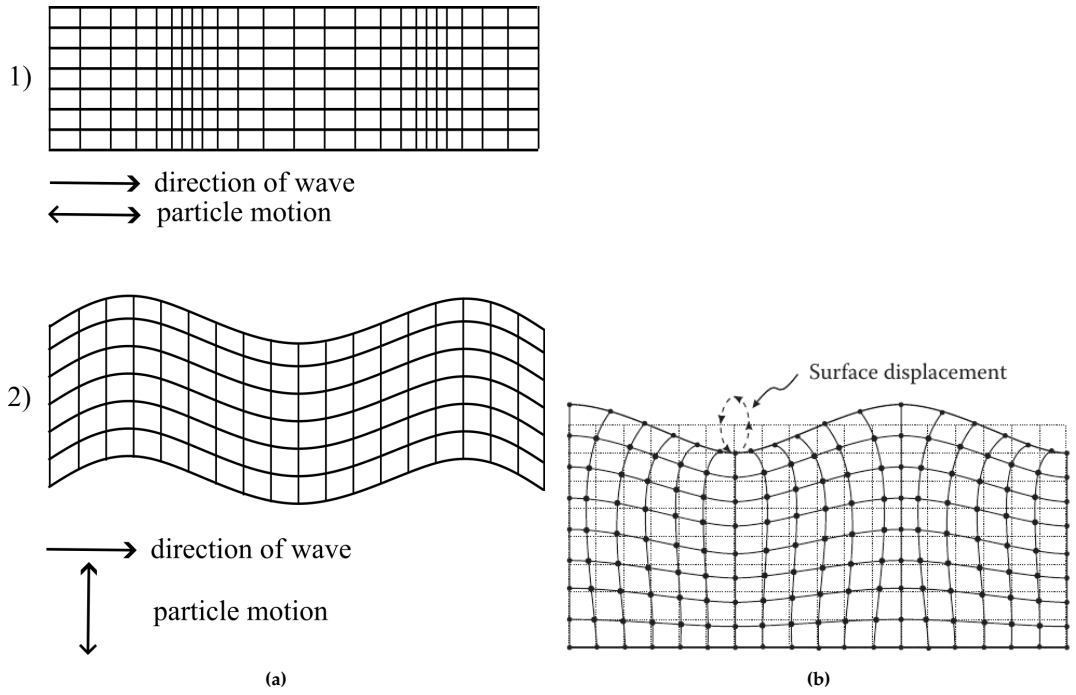

Figure B.1: a.1) The particle motion of a longitudinal wave visualized. **a.2)** The particle motion of a transverse wave visualized. **b)** The particle motion of a Rayleigh wave visualized, Figure taken from [10]

C
Artificial PA Signal

C.1. Artificial spot size

A Gaussian function, Equation C.1, is defined with an amplitude between 0 and 1 over the boundary of the imaging plane of the acoustic cavity. The location of the mean is defined by x_0, the width by c, and the amplitude by A.

$$gp(x) = Ae^{\frac{-1}{2}\left(\frac{x-x_0}{c}\right)^2} \tag{C.1}$$

It is possible to rewrite this function such that c represents the width at a certain height relative to the amplitude. This is often used to define the width at the FWHM. Here, we will define the height at which the width is defined as:

$$height = A/H \tag{C.2}$$

When H is 2, the width will be equal to the FWHM. To find the x values corresponding to a certain height, we set the height equal to Equation C.1. If we know these values of x, we can define the width as a function of c and H.

$$\frac{A}{H} = Ae^{\frac{-1}{2}\left(\frac{x-x_0}{c}\right)^2} \tag{C.3}$$

$$x_1 = c\sqrt{2ln(H)} + x_0 \tag{C.4}$$

$$x_2 = -c\sqrt{2ln(H)} + x_0 \tag{C.5}$$

$$w = x_2 - x_1 \tag{C.6}$$

$$w = 2c\sqrt{2ln(H)} \tag{C.7}$$

$$c = \frac{w}{2\sqrt{2ln(H)}} \tag{C.8}$$

And finally our Gaussian function where the width is define at a height between zero and A.

$$gp(x) = Ae^{\frac{-1}{2}\left(\frac{2\sqrt{2ln(H)}(x-x_0)}{w}\right)^2} \tag{C.9}$$

If this function is multiplied with a 1D pressure signal over time, the pressure is defined spatially and temporally. A derivative of Equation C.1 can be used to define a pressure in time. This derivative needs some tuning such that we can change the amplitude and width as we like. The amplitude gives the maximum pressure, and the width determines the signal's frequency spectrum. For our calibration, we aimed to input a broadband signal into our prism.

C.2. Pressure pulse tuning

In this section, we take the following steps to derive a formula for our pressure pulse. First, we obtain the first derivative of Equation C.1

$$gp_{,x}(x) = -A\left(\frac{x-x_0}{c^2}\right)e^{\frac{-1}{2}\left(\frac{x-x_0}{c}\right)^2} \tag{C.10}$$

The A in this function is no longer equal to the maximum amplitude. We aim to find a value for A such that the maximum amplitude is 1; we then introduce A_2 that defines the amplitude of the function. First, we have to find a value of x where the amplitude is at its maximum. If we set the formula equal to 1 and find A, we have our normalization factor. To find the x value, we set the second derivative of C.1 to zero.

$$gp_{,xx}(x) = \frac{-A}{c^2}\left(1-\left(\frac{x-x_0}{c}\right)^2\right)e^{\frac{-1}{2}\left(\frac{x-x_0}{c}\right)^2} \tag{C.11}$$

$gp_{,xx}(x) = 0$ if

$$0 = 1-\left(\frac{x-x_0}{c}\right)^2 \tag{C.12}$$

$$x = \pm c + x_0 \tag{C.13}$$

We can input this value of x in C.10 and set the equation equal to 1.

$$1 = gp_{,x}(c+x_0) \tag{C.14}$$

$$1 = -A\left(\frac{c}{c^2}\right)e^{\frac{-1}{2}\left(\frac{c}{c}\right)^2} \tag{C.15}$$

$$A = -\frac{c}{e^{\frac{-1}{2}}} \tag{C.16}$$

We use this factor to normalize the function and call this function the pressure pulse pp.

$$pp(t) = A_2 e^{\frac{1}{2}}\left(\frac{t-t_0}{c}\right)e^{\frac{-1}{2}\left(\frac{t-t_0}{c}\right)^2} \tag{C.17}$$

To define the width at a certain height, we define this height again as $\frac{A}{H}$; we then find the smallest and largest value of x that specifies this height. If we subtract those from each other, we obtain a value for the width of the function.

$$\frac{A}{H} = pp(t) \tag{C.18}$$

$$\frac{A}{H} = Ae^{\frac{1}{2}}\left(\frac{t-t_0}{c}\right)e^{\frac{-1}{2}\left(\frac{t-t_0}{c}\right)^2} \tag{C.19}$$

$$e^{\frac{1}{2}\left(\frac{t-t_0}{c}\right)^2} = He^{\frac{1}{2}}\left(\frac{t-t_0}{c}\right) \tag{C.20}$$

We can not solve easily for x; therefore, we have checked whether we could use the definition of c as defined earlier. We found a scaling factor of 0.8 for w, which creates a width almost equal to w close to a height of zero. The value w now thus represents the length of the pressure pulse. The height at which this is specified is a bit arbitrary. If we take H to be 100, then the height is specified at 1% of the amplitude. This width does not have a direct meaning but determines the band of frequencies present in the signal. In figure C.1, the relation is shown between the length of the pressure pulse and a Gaussian function having the same values for w and A.

$$c = \frac{0.8w}{2\sqrt{2ln(H)}} \tag{C.21}$$

$$pp(t) = A \cdot e^{\frac{1}{2}\left(\frac{2\sqrt{2ln(H)}}{0.8w}\right)(t-t_0)} \cdot e^{\frac{-1}{2}\left(\frac{2\sqrt{2ln(H)}(t-t_0)}{0.8w}\right)^2} \tag{C.22}$$

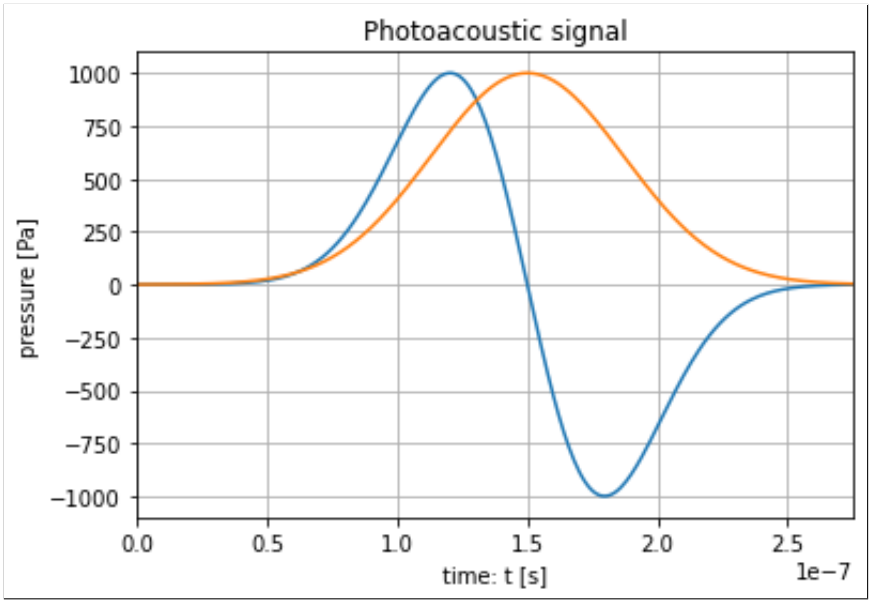

Figure C.1: The length of the pressure pulse is related to the base of a gaussian pulse with the same values for w A

D
Element Size

D.1. Sampling Theorem for the General Mesh

To approximate the value for epw needed according to the Nyquist sample theorem, the spatial frequency spectrum is calculated. Figure D.1, shows the plot of three waves spatially. Figure D.2, shows the spatial frequencies of these three waves.

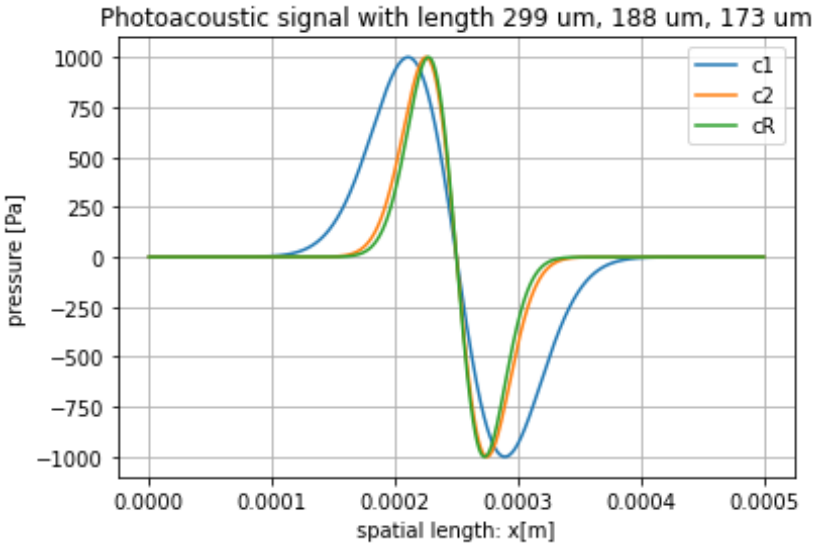

Figure D.1: The Pa signals plotted spatially for three wave types in glass.

$$ss = \frac{1}{2 * fmax} \tag{D.1}$$

$$npw = \frac{\lambda}{ss} \tag{D.2}$$

$$epw_a = \frac{npw}{4} \tag{D.3}$$

ss	m	sample size
spw	[-]	nodes per wavelength
epw_a	[-]	the number of approximated elements per wavelength

As seen in Equation D.1, to calculate the sample size, the sampling theorem is used. For the convergence study, this value needs to be converted to a value for elements per wavelength (epw). First, Equation D.1 is used to obtain the number of samples per wavelength. Since 4th-order elements are used, they can be divided by 4 to approximate the number of elements per wavelength. For the PA signal in glass defined in this project, the number of elements per wavelength can be approximated by two.

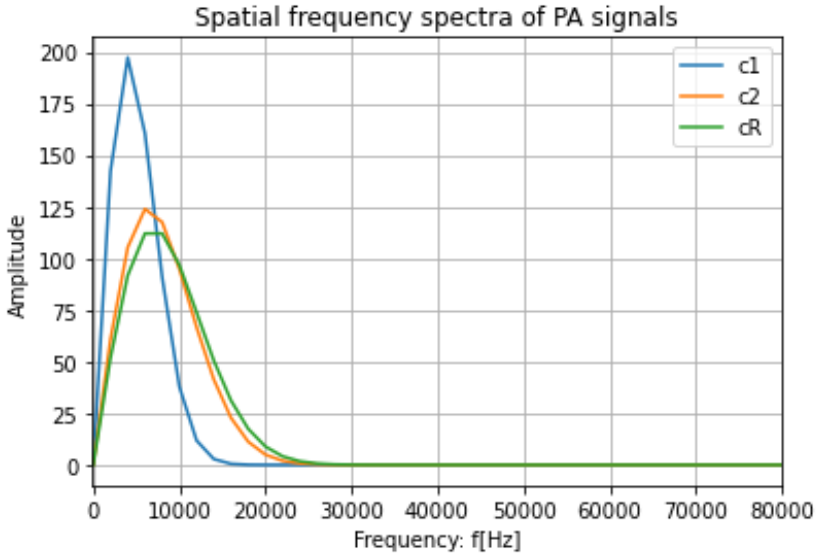

Figure D.2: The spatial frequency spectra of Pa signals plotted spatially for three wave types in glass.

D.2. Sampling Theorem for the Load Distribution

To approximate the value for epw needed according to the Nyquist sample theorem, the spatial frequency spectrum is calculated. Figure D.3, shows the frequency spectrum of the Gaussian function.

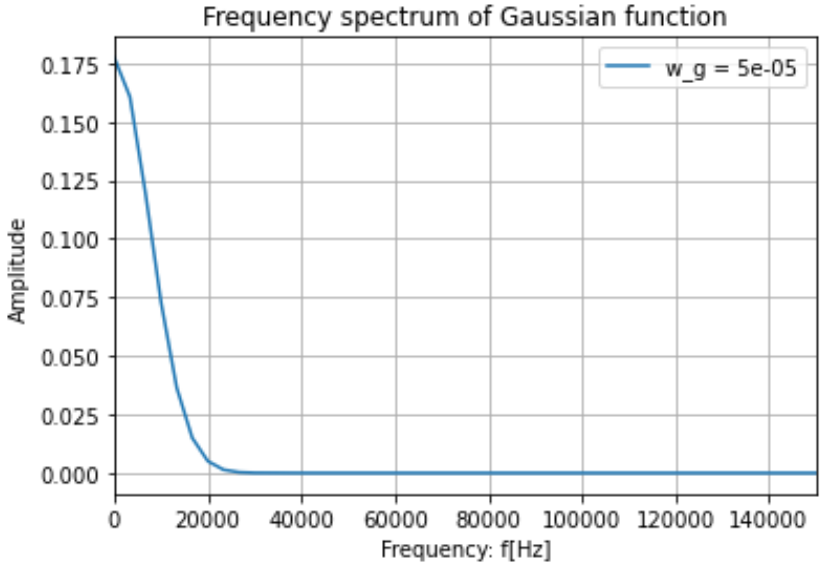

Figure D.3: The frequency spectrum of Gaussian function.

$$ss = \frac{1}{2 * fmax} \tag{D.4}$$

$$les_a = ss * 4 \tag{D.5}$$

$$ld_a = \frac{w_g}{les} \tag{D.6}$$

ss	m	sample size
les	m	load element size
ld_a	[-]	approximation for how the w_g should be discretized.

First, the sample size is calculated with Equation D.2. This model uses 4th-order elements, and the element size can thus be approximated with Equation D.2. To express this value in terms of the FWHM of the Gaussian function Equation D.2 is used. This results in $ld_a = 0.5$.

E
COMSOL Model

E.1. Wave Visualization With Second Invariant of Stress Tensor

In COMSOL presure is defined as the hydrostatic stress.

$$\sigma_{hyd} = \frac{\sigma_{xx} + \sigma_{yy} + \sigma_{zz}}{3} \tag{E.1}$$

The second invariant of the stress tensor is defined as:

$$I_1 = \sigma_{xx} + \sigma_{yy} + \sigma_{zz} \tag{E.2}$$
$$I_2 = 0.5(I_1^2 - \sigma_{xx}2 - \sigma_{yy}^2 - \sigma_{zz}^2 - \sigma_{xy}^2 - \sigma_{xz}^2 - \sigma_{yz}^2) \tag{E.3}$$
$$I_2 = 0.5(I_1^2 - (\sigma_{xx}2 + \sigma_{yy}^2 + \sigma_{zz}^2) - (\sigma_{xy}^2 + \sigma_{xz}^2 + \sigma_{yz}^2)) \tag{E.4}$$
$$I_2 = 0.5(\sigma_{xx}\sigma_{yy} + \sigma_{xx}\sigma_{zz} + \sigma_{yy}\sigma_{zz} - (\sigma_{xy}^2 + \sigma_{xz}^2 + \sigma_{yz}^2)) \tag{E.5}$$

I_1^2 is always larger than $(\sigma_{xx}^2 + \sigma_{yy}^2 + \sigma_{zz}^2)$ and always positive. Therefore, the addition due to the normal stress components is always positive.

$-(\sigma_{xy}^2 + \sigma_{xz}^2 + \sigma_{yz}^2))$ is always negative, so the addition due to the shear stress components is always negative.

If we use this for plotting the longitudinal waves and shear waves in different colors (depending on the sign), $(\sigma_{xx}\sigma_{yy} + \sigma_{xx}\sigma_{zz} + \sigma_{yy}\sigma_{zz})$ must be much smaller than $-(\sigma_{xy}^2 + \sigma_{xz}^2 + \sigma_{yz}^2))$ in the case of a shear wave. And the other way around for longitudinal waves.

F
Validation

F.1. visualization compared with data

Special interest are in the regions where peaks occur in the COMSOL measurement, but not in the PATER measurement.

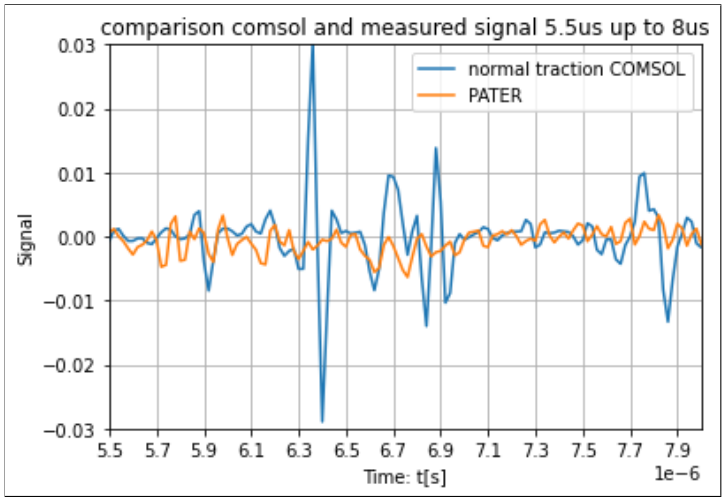

Figure F.1: Imaging process and model parts

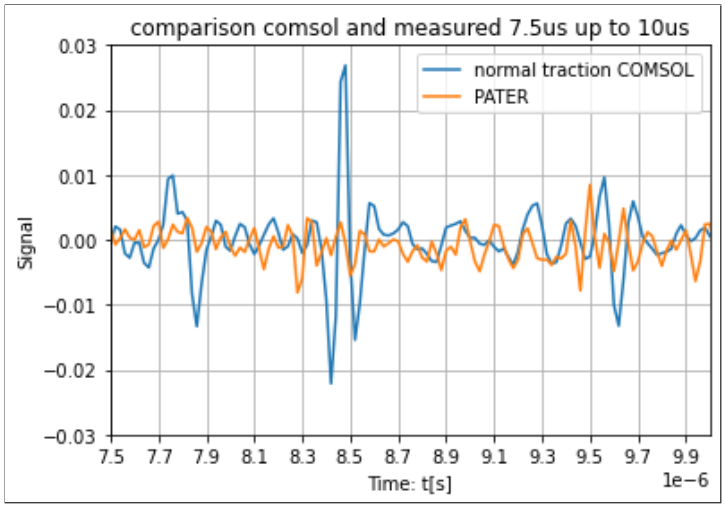

Figure F.2: Imaging process and model parts

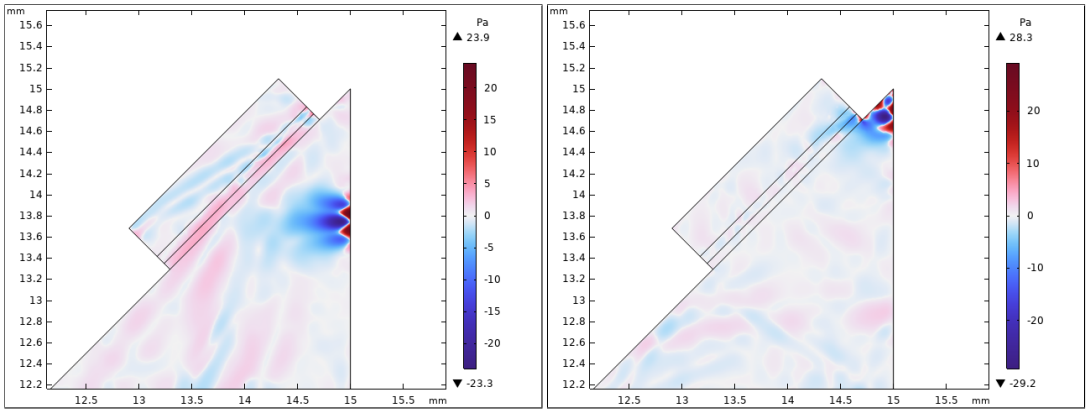

(a) 6350 ns **(b)** 6640 ns

Figure F.3

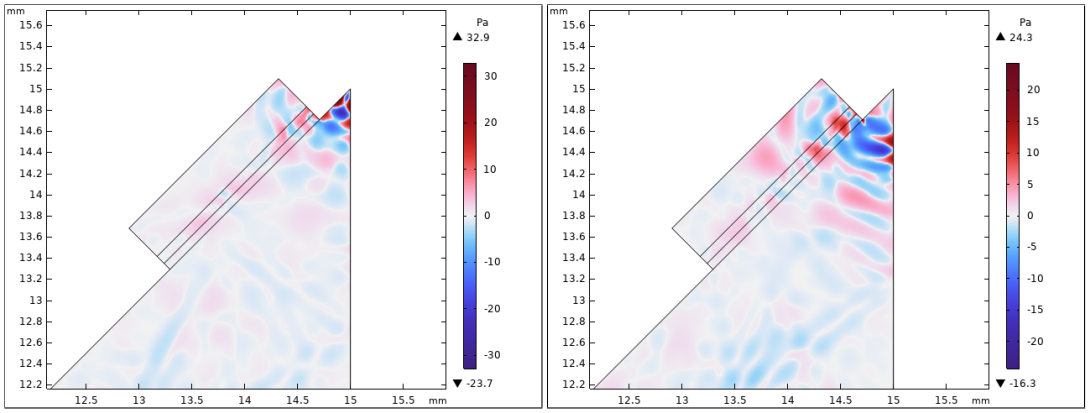

(a) 6800 ns **(b)** 6900 ns

Figure F.4

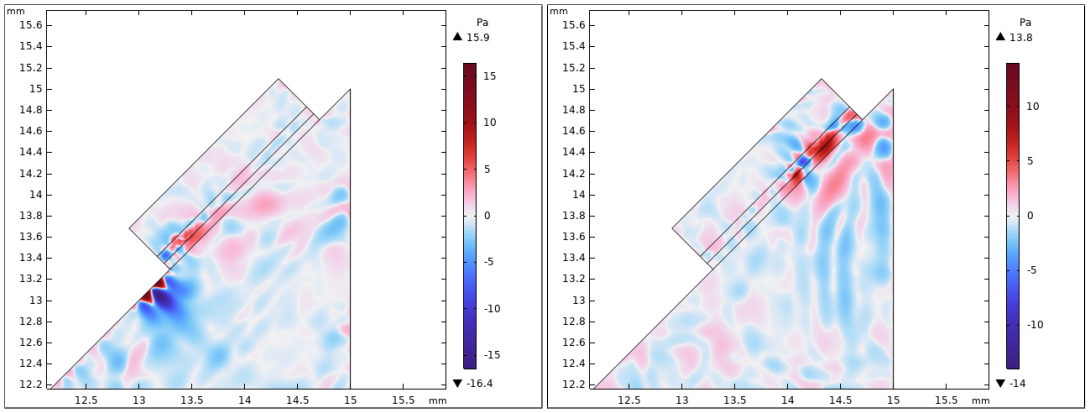

(a) 7750 ns **(b)** 8420 ns

Figure F.5

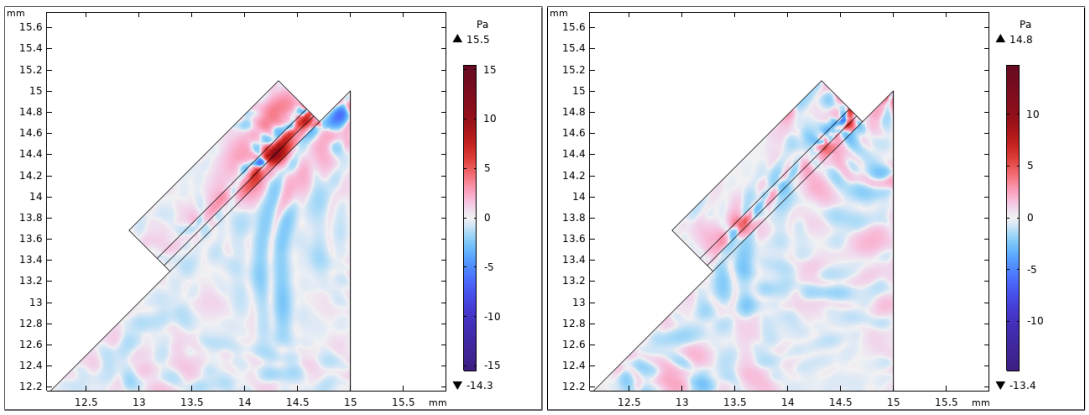

(a) 8470 ns **(b)** 8420 ns

Figure F.6

G
Cluster Computing

A script is used to run COMSOL files on DelftBLue. The following script is an example; every simulation requires different settings. There is no need to use the cluster or batch interface, just a regular COMSOL model. If a parametric sweep is performed, make sure to check the distribute sweep option. When performing a parametric sweep, an option is to set the ntasks parameter to a higher value to create multiple nodes. In this way, multiple simulations will be run in parallel.

```
#!/bin/sh
#
#SBATCH --job-name="simu1"
#SBATCH --partition=compute
#SBATCH --time=24:00:00
#SBATCH --ntasks=1
#SBATCH --cpus-per-task=48
#SBATCH --mem-per-cpu=3G
#SBATCH --account=Education-ME-MSc-ME

module load comsol/6.1

ADRESS="/scratch/cbootsma/simu1/"
RECOVERY="${ADRESS}/recovery"
MODELTOCOMPUTE="${ADRESS}/model"
INPUTFILE="${MODELTOCOMPUTE}.mph"
OUTPUTFILE="${MODELTOCOMPUTE}_output.mph"
BATCHLOG="${MODELTOCOMPUTE}.log"

comsol batch -mpibootstrap slurm -tmpdir ${RECOVERY} -prefsdir ${RECOVERY}
 -configuration ${RECOVERY} -inputfile ${INPUTFILE} -outputfile ${OUTPUTFILE}
  -batchlog ${BATCHLOG}
```